Ore Geology Reviews 150 (2022) 105150

Contents lists available at ScienceDirect

Ore Geology Reviews

journal homepage: www.elsevier.com/locate/oregeorev

Structural analysis, mineralogy, and cassiterite U–Pb ages of the Wuxu Sb-Zn-polymetallic district, Danchi Fold-and-Thrust belt, South China

Chang-Hao Xiao [a,b,*], Zheng-Le Chen [a,b], Xiang-Chong Liu [a,b], Chang-Shan Wei [a,b], Yu Wu [c], Yan-Wen Tang [d], Xin-Yu Wang [e]

[a] Laboratory of Dynamic Diagenesis and Metallogenesis, Institute of Geomechanics, Chinese Academy of Geological Sciences, Beijing 100081, China
[b] Key Laboratory of Paleomagnetism and Tectonic Reconstruction, Ministry of Natural Resources, Beijing 100081, China
[c] Beijing Research Institute of Uranium Geology, CNNC, Beijing 100029, China
[d] Stake Key Laboratory of Ore Deposit Geochemistry, Institute of Geochemistry Chinese Academy of Sciences, Guiyang 550081, China
[e] Collaborative Innovation Center for Exploration of Nonferrous Metal Deposits and Efficient Utilization of Resources by the Province and Ministry, Guilin University of Technology, Guilin 541006, China

ARTICLE INFO

Keywords:
Paleokarst infilled type deposit
Structural analysis
Cassiterite U-Pb age
Wuxu district
Danchi Fold-and-Thrust belt
South China

ABSTRACT

The Danchi fold-and-thrust belt, Guangxi, South China, contains the Mangchang, Dachang, and Wuxu large and giant Sn-polymetallic districts. It hosts more than 1.2 Mt of ore grading 1 % Sn, 6.23 Mt Zn at 2.4 %, and 1.13 Mt Sb at 1.3 %. Wuxu district is one of the Sb-Zn dominated hydrothermal districts without magmatic rocks exposing in the south of the Danchi belt. Recent drilling and exploring mining have identified a partially Sn mineralization associated with the Zn-Sb mineralization. These works provide an opportunity to evaluate the potential of tin mineralization in the south of Danchi belt and relationship among Sn, Zn, and Sb mineralization. Structural analysis suggests that the Wuxu district underwent at least three deformational phases since the Triassic. The first NE-SW shortening deformation controlled the structural framework of the Wuxu district and is expressed by NW-verging thrusts and folds, axial-plane cleavages around the core of the Wuxu anticline, transverse joint sets on the limbs of the Wuxu anticline, and dilational zones in the bedding-fractures. Afterward, an E-W extension stress field produced NS-striking normal faults and reactivated pre-existing NNW-striking faults which were expressed by sinistral top-to-the north sense of shear. During this deformation, some low order dilational spaces of the NW-striking faults and bedding-fractures formed and a *syn*-kinematic deposition of minerals in these hosting structures to form the ore shoots. The NNW-striking faults, axial-plane cleavages, and large dilational jogs controlled the subvertical large veins in the Jianzhupo deposit. The conjugate joints and inter-bedding fractures in the limb of the Wuxu anticlinorium controlled the branching veinlets and stratiform, paleokarst infilled ores in the Bawang deposit. The post-ore EW-striking faults are not obvious and displaced preceding two-phase structures and ores. Three primary paragenetic stages of hydrothermal process have been recognized: (I) Sphalerite dominated + massive pyrrhotite with euhedral pyrite porphyroblasts, (II) Cassiterite + siderite + arsenopyrite dominated with minor scheelite + quartz + fluorite, and (III) Jamesonite + stibnite + sulfosalt + carbonates. Cassiterite U-Pb dating provided a lower intercept age of 90.2 ± 3.1 Ma and 90.6 ± 4.6 Ma for the Jianzhupo and Bawang deposits, respectively. These two ages are consistent with the chronological data of tin-sulfides and ore-related felsic intrusions in the Danchi fold-and-thrust belt, South China. Our studies coupled with previous gravity data suggests a distal magmatic-hydrothermal infilling tin-polymetallic district and indicates that the Wuxu district has great potential for additional tin mineralization.

1. Introduction

China is the world's largest tin producer, which held about 25.6 percent of the world's tin reserves and accounted for 28.5 percent of the world's production of tin in 2019 (U.S. Geological Survey, 2021). South China hosts many thousands of base metal deposits and occurrences and

* Corresponding author at: Laboratory of Dynamic Diagenesis and Metallogenesis, Institute of Geomechanics, Chinese Academy of Geological Sciences, No. 11, Minzudaxue South Road, Beijing 100081, China.
E-mail address: xiaochanghao1986@126.com (C.-H. Xiao).

https://doi.org/10.1016/j.oregeorev.2022.105150
Received 14 December 2021; Received in revised form 27 September 2022; Accepted 5 October 2022
Available online 8 October 2022

accounts for about 85 percent of China's production of tin (Mao et al., 2019). The Youjiang Basin produced approximately 60 percent of the tin in South China (Fig. 1A, B). Almost all of the tin deposits formed along the boundary faults of the Youjiang Basin, such as the world class Dachang, Gejiu, and Dulong Sn-dominant polymetallic districts which are the three giant districts in the Youjiang Basin (Fig. 1C). As of 2019, the Danchi fold-and-thrust belt contains resources of approximately 1.36 million tons of Sn metal, 6.23 million tons of Zn metal, 1.25 million tons of Pb metal, 1.13 million tons of Sb metal, and other metal (Cu, Ag, In, Ge) (Ye and Pan, 1994; Zhang et al., 2018). Tin mining in the Danchi fold-and-thrust belt dates back to the 1130 s, but modern industrial mining started in the 1960 s with an annual production of about 1000 t Sn metal (Ye and Pan, 1994). Despite such a long history of utilization and investigation, various questions regarding the genesis of the deposits in the Danchi belt, including their age and their relationship with the tectonic evolution and the structural styles are still debated (Fu et al., 1991, 1993; Ye and Pan, 1994; Han et al., 1997; Peng et al., 1997; Jiang et al., 1999; Fan et al., 2004; Cai et al., 2007; Guo et al., 2018; Huang et al., 2019; Wang et al., 2019; Zhao et al., 2021). The debates largely focus on whether the ores are related to submarine exhalations during a Devonian or Late Cretaceous magmatic-hydrothermal event (Han et al., 1997; Guo et al., 2018; Zhao et al., 2021). One of the most significant orebodies is the No. 100 orebody, a single orebody that contains 218, 200 tons of tin metal formed in the reef limestone in the Dachang district with no obvious alteration of the hosting reef limestone. The orebody displays a dominant northwest trend (320–330°) with variable dip (34–55° from top to bottom) (Zhang et al., 2014). The obvious characteristic is the curved shape of the orebody. Most researchers suggested that the ore-forming fluids were derived from the Late Cretaceous felsic intrusions and infiltrated into the fractures in the reef limestone (Yao and Qing, 2002; Cai et al., 2007; Xiao, 2018). Other researchers have proposed that the ore-forming fluid flowed upward along the NW-trending faults and were deposited in the cavities of the reef limestone (Su et al., 2007; Zhang et al., 2014). If there are contemporaneous

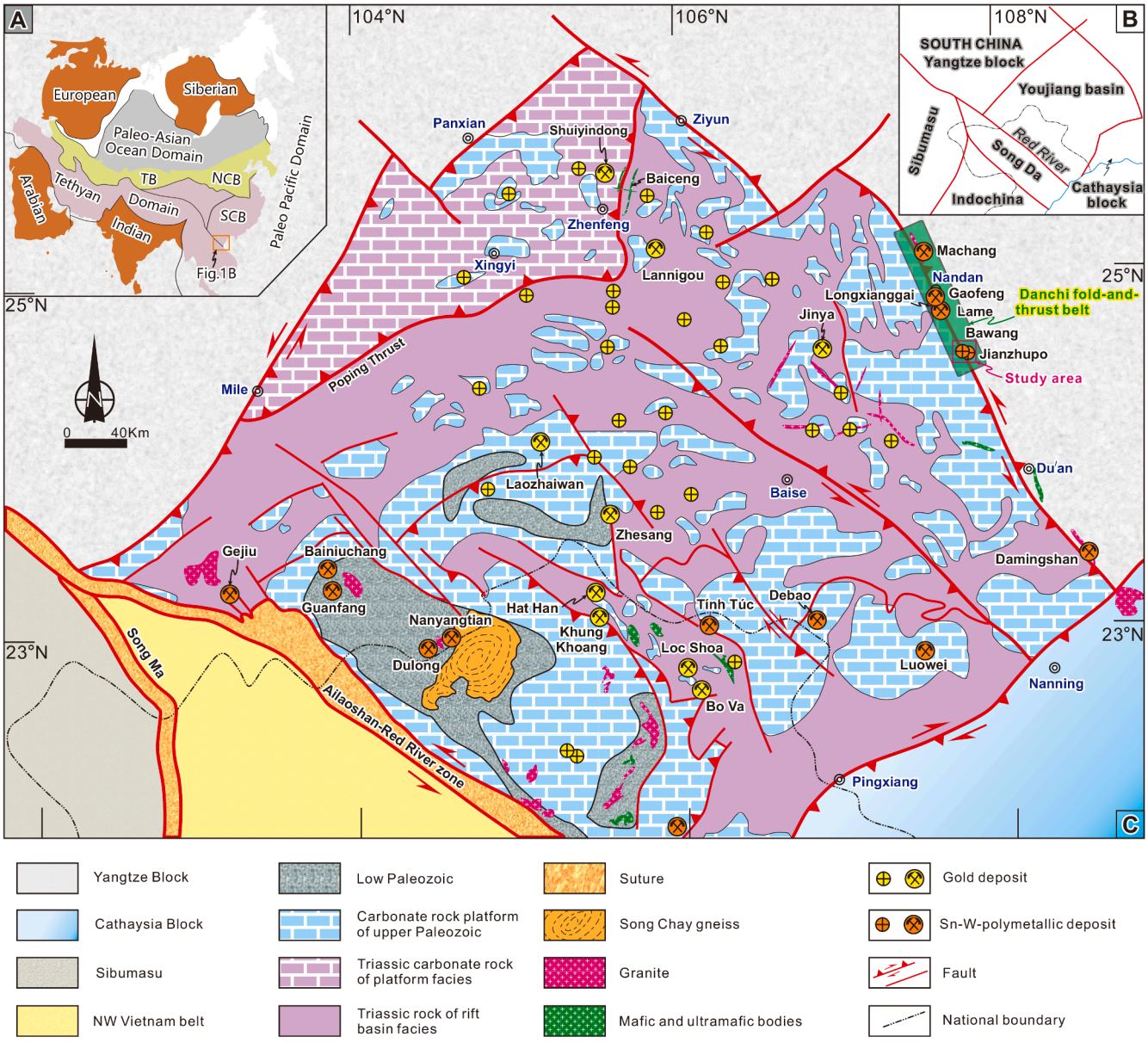

Fig. 1. (A) Tectonic map of Asia showing continental blocks and bounding sutures (modified after Cawood et al., 2018). (B) Geological location of the studied area. (C) Schematic geological map of the Youjiang Basin and the distribution of Sn and W polymetallic deposits and gold deposits (modified after Chen et al., 2012, 2014,2019; Nevolko et al., 2017; Xiao et al., 2018a, b; Mao et al., 2019). The green rectangle in the Fig. 1C represent the location of the Danchi fold-and-thrust belt. TB-Tarim Block, NCB-North China Block, SCB-South China Block.

paleokarst infilled type tin deposit in the Danchi belt, then it is important for us to reconceptualize the tin mineralization. Fortunately, Zn-Fe-Sn orebodies in the paleokarst were discovered in the Bawang deposit and quartz vein-type tin orebodies were recently discovered at −180 m within the Jianzhupo deposit, Wuxu district, southeastern Danchi fold-and-thrust belt, respectively. These orebodies provide an opportunity to test whether tin mineralization was coeval with the emplacement of the intrusion in the south of the fold-and-thrust belt and to discuss the relationship among Sn, Zn, and Sb mineralization. In this contribution, we present ore mineralogical, textural, the structural analysis, and laser ablation-inductively coupled plasma-mass spectrometry (LA-ICP-MS) U-Pb ages of cassiterite. Our new data are used to constrain the timing of the tin mineralization and the structural controls on the mineralization. We also offer an implication for understanding regional tin mineralization and guiding the further exploration in the Danchi fold-and-thrust belt.

2. Geological background

2.1. Regional geology

The South China Block, at the transition between the Tethyan and western Pacific domains, is considered to be a result of the early Neoproterozoic amalgamation between the Yangtze Block in the northwest and the Cathaysia Block in the southeast along the Jiangnan Orogen (Fig. 1A, B; Charvet et al., 1996). Subsequently, the South China Block experienced early Paleozoic intraplate magmatism, the spreading and closure of the Paleo-Tethyan Ocean from the Devonian to Triassic, and the subducting Paleo-Pacific plate from the Late Paleozoic to Mesozoic, followed by regional uplift caused by Cenozoic collision between the Indian and Eurasian continents (Zhang et al., 2013; Faure et al. 2017; Li et al., 2018, 2019,2020; Wang et al., 2020a; Shu et al., 2021). At a local scale, the Emeishan large igneous province is exposed in the middle of the Youjiang Basin (Wang et al., 2020a). The Youjiang Basin in the western part of the South China Block is diamond-shape and controlled by the Ziyun-Du'an fault in the northeast, Pingxiang fault in the southeast, Ailaoshan-Red River fault zone in the southwest, and Shizong-Mile-Panxian fault in the northwest (Fig. 1C; Xiao et al., 2018a, b; Chen et al., 2019). It hosts about 900 t gold and 4,420,000 t Sn, as well as large quantities of Sb, Pb, Zn, and Cu (Cai et al., 2007; Cheng et al., 2013). The regional metallogeny closely parallels the multiple cycles of tectonic evolution of the Youjiang Basin (Mao et al., 2019, 2020).

The nature of the basement in the central part of the Youjiang Basin is still unknown. The sedimentary successions are different on both sides of the Poping thrust (Fig. 1C). The pre-Devonian strata are only exposed in the southern part of the Youjiang Basin. From east to west (from Nanning to Debao to Maguan), the Cambrian strata transitions from the deep-water flysch to slope basin facies carbonate to shallow-water dolomite. Minor Ordovician flysch and seafloor keratophyre distributed in the Damingshan district. Owing to the Early Paleozoic intracontinental orogeny, related to collision of the South China Block with Gondwana (Li et al., 2016), early Paleozoic granitoids distributed along the southeastern margin of the Youjiang Basin, such as the Damingshan and Qingjia plutons (Zhou et al., 2017; Wang et al., 2020b). Accompanying NS-striking compression (D1), a fold-and-thrust belt formed with deformational fabrics weakening from southeast to northwest (Gao, 2020). The mineralization associated with this orogeny represent by the Debao skarn Cu-Au (-Sn) deposit in the southern Youjiang Basin (Fig. 1C; Chen et al., 2021). In response to this intraplate orogeny, an angular unconformity between the Devonian-Triassic strata and pre-Devonian deformed rocks is widely developed in the southeastern of the Youjiang Basin (Li et al., 2016; Qiao, 2016; Gao, 2020; Wang et al., 2020a, b). The Devonian-Triassic strata is characterized by isolated carbonate platforms surrounded by deep-marine pelite, chert, limestone, and large volumes of mafic and intermediate volcanic rocks associated with spreading of the Paleo-Tethyan Ocean (D2) (Zeng et al., 1995; Chen et al., 2019; Duan et al., 2020). The amalgamation of Indochina and the South China Block during the latest Permian-Middle Triassic (D3) and the Paleo-Pacific westward subduction from the Permian (D4) led the Youjiang Basin to undergo NE-SW- and NW-SE-directed compression (Li et al., 2018). During the third-phase deformation (D3), NW-directed thick-skinned and thin-skinned fold-and-thrust systems formed to the north and south of the Baise fault, respectively. The ductile deformation developed in the Song Chay gneiss at 236 Ma (Maluski et al., 2001). Due to the influence of the pre-existing NE-striking structures (such as the Pingxiang fault), the deformation in the Youjiang Basin related to the fourth-phase of deformation (D4) is relatively weak compared to D3 deformation. The D4 deformation is expressed by NW-verging thrusts and folds, and conjugate sets of *N*-striking sinistral and E-striking dextral faults (Li et al., 2020). Owing to the change of subduction angle and slab rollback (D5), the Early Cretaceous concealed granites (140–130 Ma, inherited zircon U-Pb ages, Zhu et al., 2016) and associated disseminated gold deposit (141–134 Ma, calcite Sm-Nd (Su et al., 2009), apatite Th-Pb ages (Chen et al., 2019), and rutile SIMS U-Pb (Gao et al., 2021)) formed in the middle of the Youjiang Basin. Subsequent extension causing by the steep subduction of the Pacific Plate during the 120–70 Ma (D6) led to magmatic activity and associated magmatic-hydrothermal Sn-W-polymetallic deposits developed in the Youjiang Basin (Cheng et al., 2016; Xiao et al., 2018a, b; Mao et al., 2019, 2021; Suo et al., 2020).

2.2. Geology of the Danchi fold-and-thrust belt and Wuxu district

The Danchi fold-and-thrust belt is located in the middle of the Ziyun-Du'an fault-fold belt (Fig. 1C), which is adjacent to the Jiangnan Massif in the northeast (Fig. 2A). It consists of 2,600 m of Lower Devonian to Tertiary flysch sediments, carbonate, and minor volcano-clastic rocks (Fu et al., 1993; Cai et al., 2007). No Jurassic or Cretaceous strata developed and the basement is not exposed in this area (Guo et al., 2018). Since the Devonian, this region experienced D2 through D6 events resulting in formation of SW-verging thrusts and folds superimposed by a series of NE-, SN- and EW-striking structures (Fig. 2A; Cai et al., 2012; Wu et al., 2019). The intersection of the NW–SE-trending folds by faults was the locus for igneous intrusion and subsequent ore formation (Fu et al., 1993; Cai et al., 2012). Cretaceous granite porphyry dikes (89.1 ± 0.9 Ma, zircon U-Pb ages, Wu et al., 2020) and biotite granite (Longxianggai pluton) and granite/diorite porphyry dykes (99–88 Ma, zircon U-Pb ages, Cai et al., 2006; Liang et al., 2011; Xiao, 2018; Wang et al., 2019; Wu et al., 2020; Guo et al., 2021) in the Mangchang and Dachang districts, respectively. The Cretaceous greisen Zn-Sn (Mangchang district) and skarn Sn-Zn (Dachang district) polymetallic mineralization distributed in the north and middle of the Danchi fold-and-thrust belt, respectively. The hydrothermal Pb-Zn (Beixiang district) and Sb-Zn (Wuxu district) polymetallic mineralization distributed in the south of the Danchi fold-and-thrust belt (Fig. 2A).

The Wuxu district underwent NE–SW-directed continental rifting during the Devonian-Carboniferous (D2), SW-verging fold-and-thrust and overprinted by later NW-verging fold-and-thrust from the Permian to the Early Cretaceous (D3–4), and two episodes of extension during the Cretaceous (D5–6). The sedimentary successions in the Wuxu district consist of the following: The Devonian black pyrite-enriched mudstones, marlstones, siliceous rocks, limestones, and minor siltstones; the Carboniferous gray shallow-sea platform limestone and dolomites in the east of the Wuxu anticline to the dark deep-water slope-basin mudstones, siliceous rocks, calcirudytes with minor chert banding in the west; the Permian gray shallow-sea platform limestones in the east to deep-water slope-basin siliceous rocks and clastic rocks in the west; and finally, the Triassic calcareous shale and siltstone.

The NNW–SSE-trending Wuxu anticlinorium and Bayue syncline, the NNW-, NE-, and EW-striking faults are the main structures in the Wuxu district (Fig. 2B). The Wuxu anticlinorium has a NNW–SSE strike (355°) and gentle dip (7°) (Figs. 2C, 3A). Bedding poles (S_0) measured on the

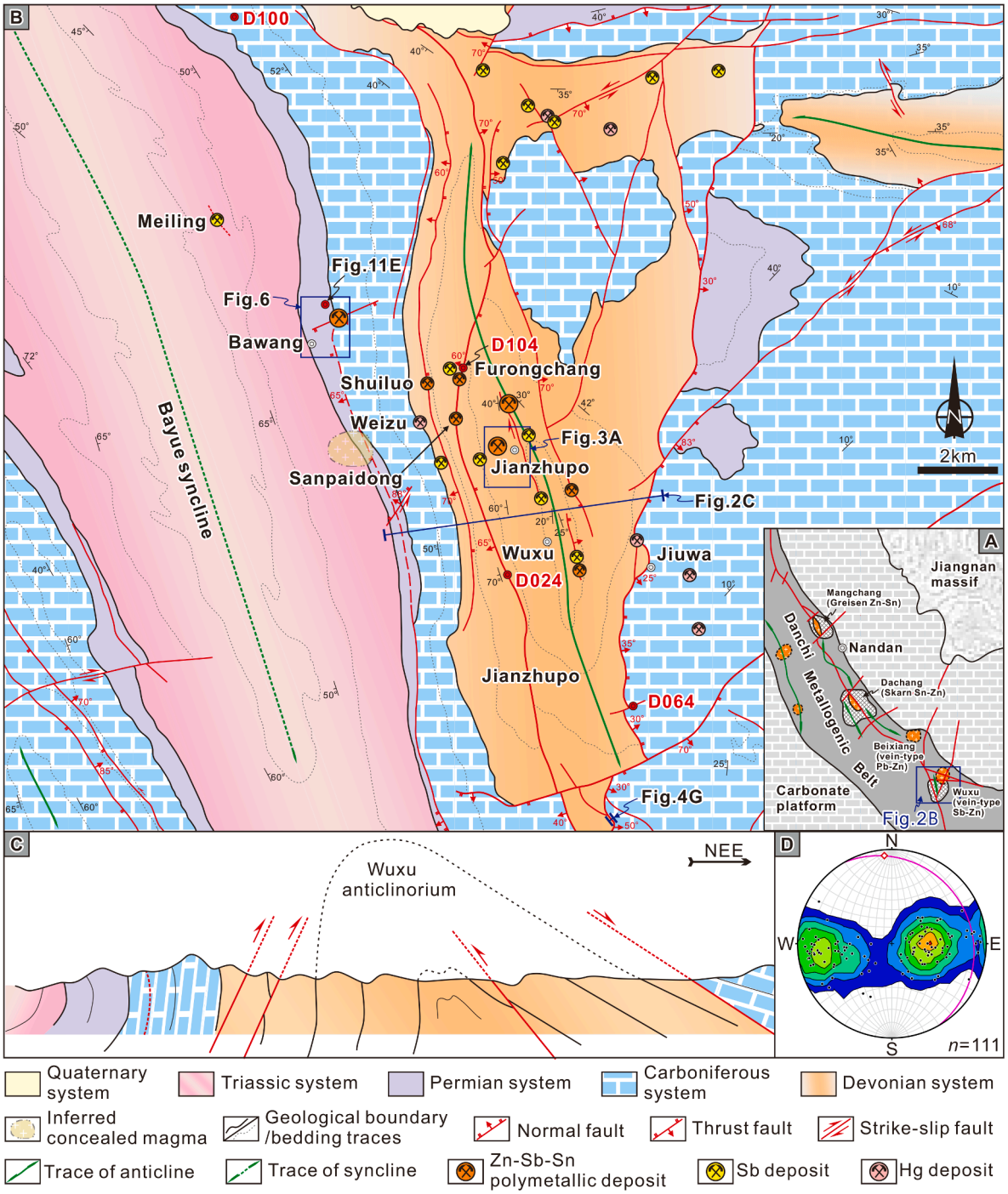

Fig. 2. (A) Schematic geological map of the Danchi fold-and-thrust belt and the distribution of magmas and districts (modified after Han et al., 1997). (B) Schematic geological map of the Wuxu district and the distribution of Zn-Sn polymetallic deposits, Sb deposits and Hg deposits. (C) Geological profile of the Wuxu anticline. (D) Stereonets (lower hemishere, equal angle) of Wuxu anticline, based of new mapping and historical measurements from Hao (2012). The great pink circle represents the strike and dip of the axial plane. The red square on the great circle represent the trend and plunge of fold axis.

fold limbs define a pattern of asymmetric folding about shallowly NE dipping fold axes (Figs. 2D, 4A, B). Oblique axial-planar cleavage (S_1) or crenulations are observable within black mudstones and boudins formed in the more competent layers (such as siltstones) due to bedding-shear during the Wuxu anticlinorium development (Fig. 4A–C). The NNW-striking faults, bedding fractures, axial-planar cleavages and conjugate joints are the major ore-bearing structures (Figs. 3, 4D–H, 5–6). From west to east, the NNW-striking Bawang, Shuiluo, Sanpaidong, Jianzhupo faults and NNE-striking Jiuwa fault develop within the core of the Wuxu anticline and control the distribution of the Bawang Zn-Fe(-Sn), Shuiluo-Weizu Hg-Sb, Sanpaidong-Furongchang Pb-Zn-Sb, Jianzhupo Sb-Zn, Jiuwa Hg deposits (Fig. 2B). NE–SW- and E–W-striking faults occur in the Wuxu district which cut the NNW–SSW-striking faults. Most of the E–W-striking dextral faults cut the ores in the Wuxu district except that the NEE-striking dextral faults are the major ore-bearing faults (Fig. 2B). There are no magmatic rocks exposed in the study area, but gravity survey and controlled source audio-frequency magneto-telluric (CSAMT) sounding works suggest that a concealed intrusion is likely sitting at 3 km depth to the south of the Bawang deposit (Zhao et al., 2020).

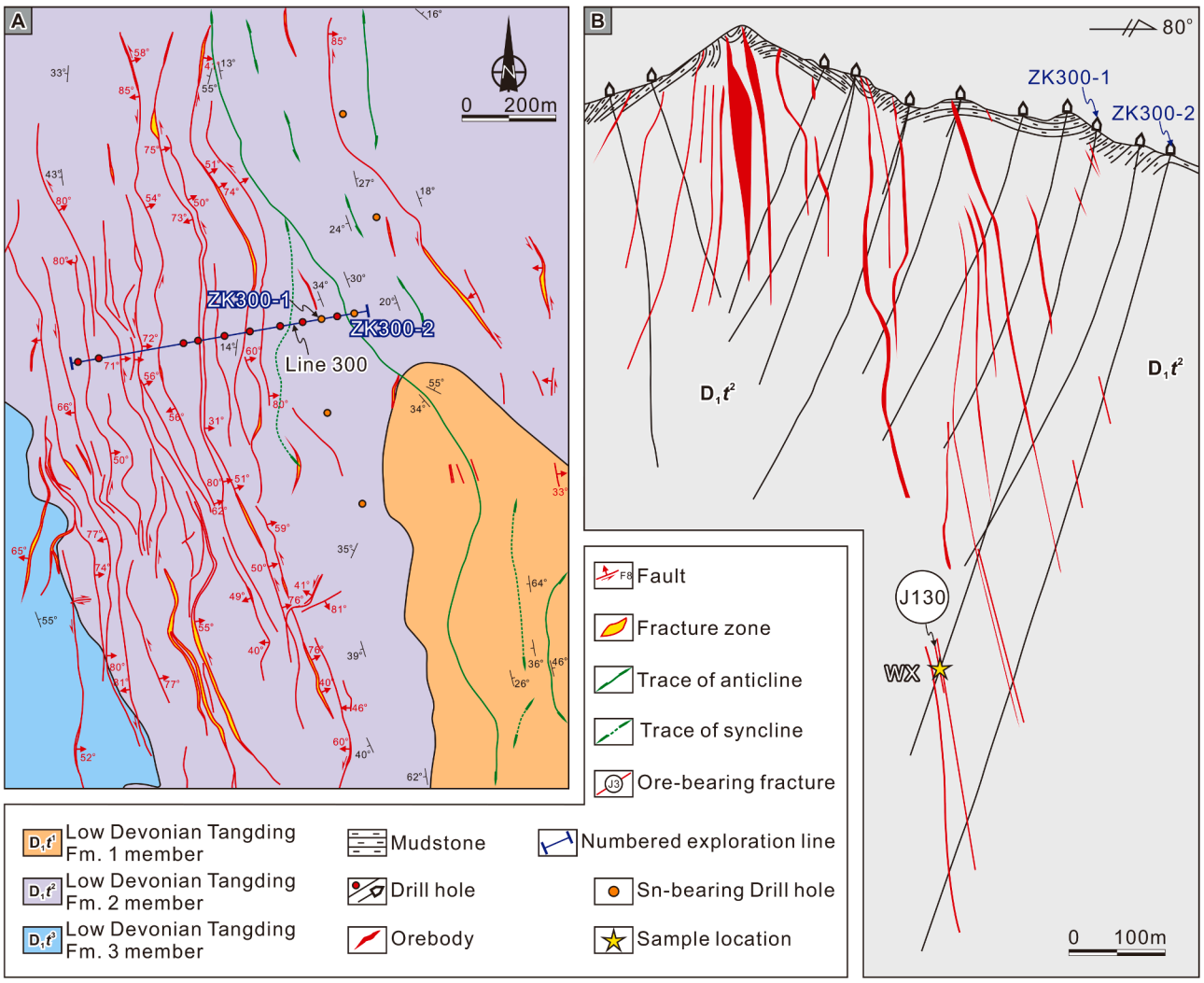

Fig. 3. (A) Schematic geological map of the Jianzhupo Sb-Zn-polymetallic deposit and the distribution of orebodies and faults (modified after Liu et al., 2020a). (B) Line 300 prospecting profile (modified after Chang et al., 2016).

3. Ore deposit geology

3.1. Jianzhupo Sb-Zn polymetallic sulfide deposit

The Jianzhupo deposit, a large Sb-Zn deposit, occurs in the center of the Wuxu district (Fig. 2B). It contains reserves of about 210,000 t of Sb, 510,000 t of Zn, 168,000 t of Pb and 852 t of Ag (Cai et al., 2014). Mining activities for Ag date back to the Qing Dynasty (1636–1912 CE). Seventy-two orebodies in the Jianzhupo deposit have been identified in the core and west of anticlinorium (Fig. 3). Orebodies are hosted by the Lower Devonian Tangding Formation (D_1t) mudstone, shale, and marlstones, with minor fine sandstone and limestone. The second member (D_1t^2) black pyrite-bearing mudstones and the third member (D_1t^3) argillaceous siltstones are the main ore-bearing strata (Fig. 3). Mineralization is controlled mainly by NNW–SSE striking, steeply-dipping (70°–85°) faults, conjugate joints, and inter-bedding fractures (Figs. 3, 4A, D–H). The orebodies comprise a series of parallel or sub-parallel large mineralized veins with thicknesses typically ranging from a few centimeters to meters and branching veinlets (Figs. 3B, 4D–F).

Field and underground observations show that the mineralization process could be divided into three stages. The pre-mineralization quartz (*Qz1*)-pyrite (*Py1*) veins (Stage i) underwent deformation during the Wuxu anticlinorium development, and were enveloped by jamesonite (*Jam*)-pyrite (*Py3*)-calcite (*Cc*) veins along both sides of the *Qz1-Py1* vein, or were crosscut by the *Jam*-manganocalcite (*Mn-Cal*) and *Jam*- ferroan sphalerite (*Sp*)-pyrite (*Py3*)–*Cc* veins (Fig. 5A, B, F). Stage ii is associated with the formation of cassiterite (*Cst*)-*Sp*-pyrite (*Py2*)-quartz (*Qz2*) veins with minor chalcopyrite (*Cp*) (Fig. 5D, E, G–H, J). The cassiterite is generally fine-grained (0.2–0.1 mm) and is subhedral to euhedral with boundaries of *Py2* (Fig. 5H). The tiny *Sp* drop-shaped inclusions could be found in *Cst* grains under both reflected and transmitted light (Fig. 5L). Black holes distributed on the *Cst* grains under the backscattered electron image which show lighter zones in the cathodoluminescence (CL) images and the *Jam* filled into the fractures of the *Cst* grains (Fig. 5K). Parts of the *Cst-Py2-Qz2* vein of stage ii extended from the wall rock into the vein and the *Jam-Py3*-manganosiderite veins of Stage iii grow on the tip of minerals of the Stage ii (Wang, 2012). The stibnite (*Stb*)-*Jam-Py3-Cc-Mn-Cal*-ankerite veins of Stage iii crosscut the veins of Stage ii (Fig. 5D–E). The stibnite and jamesonite grew on the wall rocks or radially infilled into the fractures of *Sp* (Fig. 5I–J). Parts of faint yellow jamesonite were replaced by gray stibnite (Fig. 5J). The hydrothermal alteration includes silicification, pyritization, and carbonization.

3.2. Bawang paleokarst infilled type Zn-Fe-Sn polymetallic deposit

The Bawang deposit, a paleokarst infilled type deposit, occurs in the west limb of the Wuxu anticline. Until 2020, it contains reserves of about

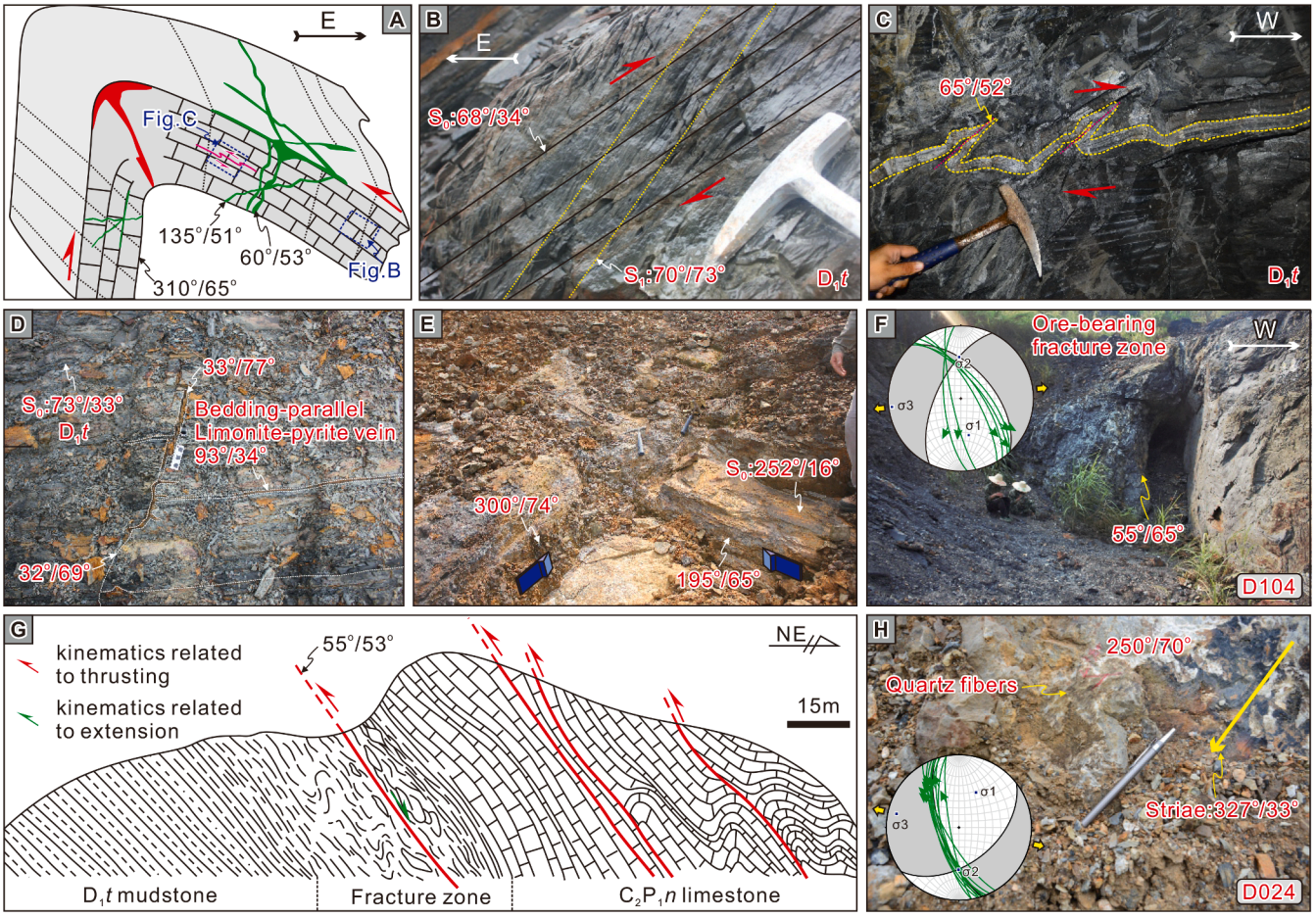

Fig. 4. The characteristic of pre-mineralization structures in the Wuxu ore field. (A) Schematic map of the Wuxu anticline and the distribution of the ores. The cleavages (B), crenulations (C), ore-bearing bedding-fractures (D) and transverse joint sets (E) formed on the limbs of the Wuxu anticlinorium. (F–G) Field photographs and cross section display the NW-striking thrust faults. The striations and mineral fibers suggest these underwent twice deformation. The oblique slickenlines overprinted on the fault planes. Stereographic plots (lower hemishere, equal angle) of the later deformation document a near-EW direction extension regime.

58,000 t of Fe, 42,133 t of Zn, 4248 t of Sn, and 142,000 t of S, as well as large quantities of Ag (27 t), Cd (418 t), In (207 t), As (7675 t), Ga (34.8 t) (SCSH, 2021). Small mining activities for Sn and Ag date back to the Qing Dynasty (1912–1636 CE) while modern industrial mining started in 2006 for Fe orebodies. The Sn-Zn orebodies were first found below 502 m level since 2017. The sedimentary rocks consist of the Middle Carboniferous-Lower Permian Nandan Formation (C_2P_1n) of dark deep-water slope-basin calcirudytes, limestones, siliceous rocks, with minor chert banding. From the top to the bottom, the Nandan Formation divided three members in the deposit: the fourth member ($C_2P_1n^4$) consist of dark thick-bedded calcirudytes; the third member ($C_2P_1n^3$) is comprised of limestone with interbedded dolomitic limestone overlying interbedded siliceous rocks and limestone; the second member ($C_2P_1n^2$) represented by the 30-to 60-cm-thick gray fine crystalline limestone. The Middle-Lower Permian Sidazhai Formation ($P_{1\text{-}2}s$) is a limestone with interbedded siliceous rocks and mudstone; the Upper Permian Linghao Formation (P_3lh) gray thin-bedded mudstone with interbedded siltstone and tuffite and minor siliceous rocks; the Lower Triassic Shipao Formation (T_1s) dark gray thin-bedded mudstone. All of the strata dip to the west (240°–290°) at 35°–82° (Fig. 6). The EW- and NS-striking faults are the main structures in the deposit. The EW-striking F5 normal fault dips S at 72° and controls the distribution of the EW-trending orebody I (Figs. 7A, 8, 9A–B). The NS-striking faults are steeply-dipping (50°–85°). The NS-striking F3 normal fault dips to W at 55°–66° that controls the NS-trending orebody II (Fig. 9C).

The orebody I contains approximately 90 % of the reserves. Most of orebody are distributed in cavities of the Nandan Formation ($C_2P_1n^4$) calcirudytes and the contact between calcirudytes and Sidazhai Formation ($P_{1\text{-}2}s$) flint-bearing calcarenite and bioclastic limestone (Figs. 7C, 8, 9A). The level drifts and drill holes revealed that each single orebody dips S at 76°–86° and orebody I extends from NE to SW (Figs. 7–8). Ore types are divided into oxidized, mixed, and sulfide ores. The oxidized and mixed ores transition zone, and sulfide and mixed ores transition zone located at 502 m and 220 m, respectively (Fig. 7A).

Ore mineralogy and microtextural studies show that the ore-forming process can be divided into thermal transformational, hydrothermal, and supergene oxidation stages. Based on mineral paragenetic sequences, the hydrothermal stage could be further divided into three substages as follows.

Thermal transformational stage is associated with the formation of massive pyrrhotite (*Po1*), and porphyroblastic pyrite (*Py1*). One of the most common forms of *Py1* observed in hand species and polished sections is that of discrete and very large cubic porphyroblasts (Fig. 9E, H–I). The crystals, up to 1 cm across, are commonly euhedral and were replaced by sulfides-quartz-siderite veins along the edge of the crystals (Fig. 9H).

Substage i of hydrothermal stage is associated with the formation of enhudral ferroan sphalerite masses (*Sp1*) with minor pyrrhotite laths, chalcopyrite blebs, stannite, and cassiterite (*Cst1*) (Fig. 9 J–M). The *Po1* was replaced by the *Sp1* and was crosscut by the ferroan sphalerite (*Sp2*)-arsenopyrite-pyrite (*Py2*)-marcasite-quartz-siderite veins (Fig. 9H–I). The coarse-grained *Sp1* coexisted with needle-shaped

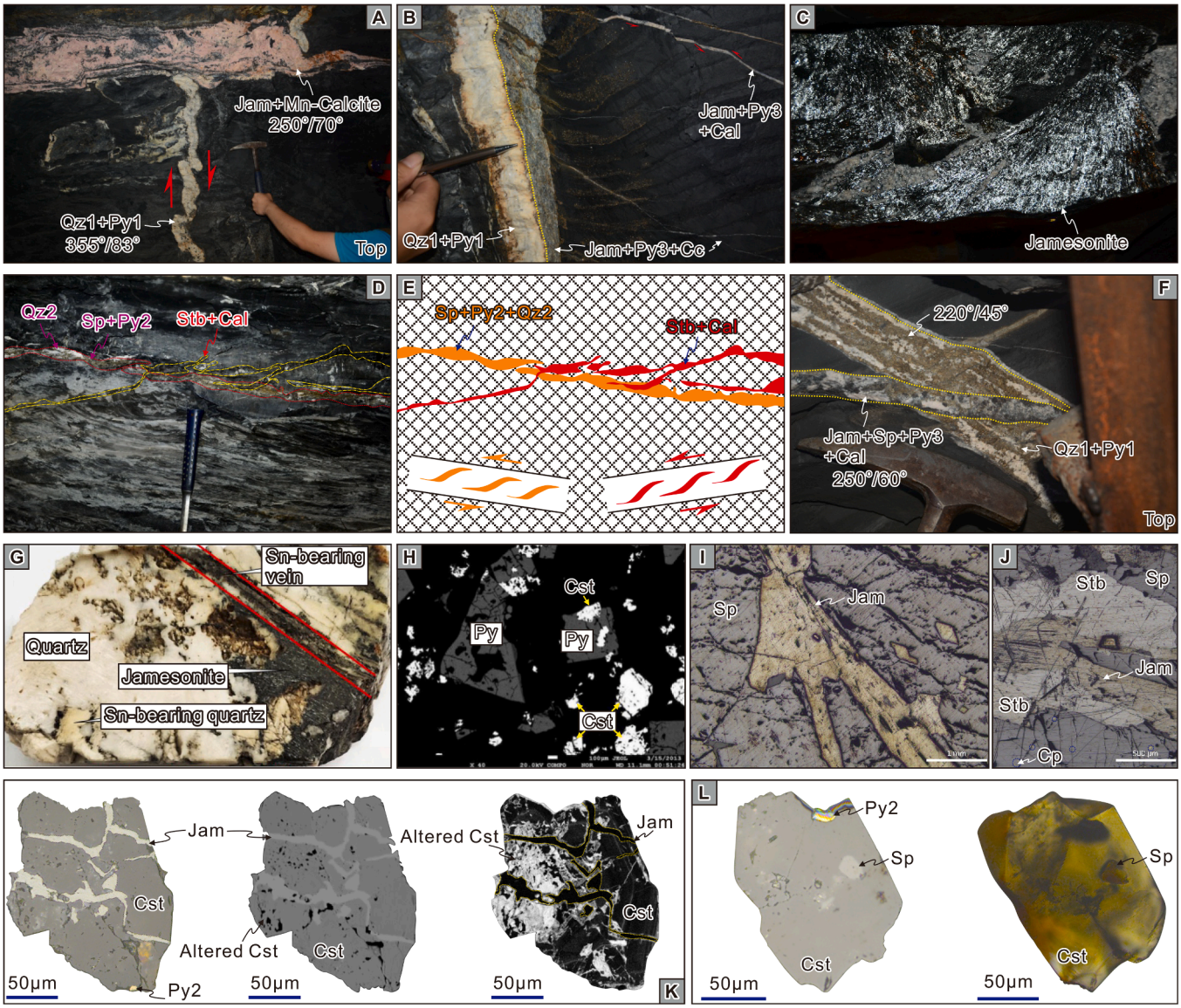

Fig. 5. (A) The deformation pyrite-quartz veins were cut by the jamesonite-tetalite large veins. The crenulations indicated a dextral shear. (B) The jamesonite-pyrite-calcite veins form along the pyrite-quartz veins. The geometry of intervening rhomboidal space infilled with jamesonite, pyrite and calcite indicate a sinistral movement. (C) The radial jamesonites growth on the fracture surface. (D–E) The stibnite-calcite vein crosscut the ferroan sphalerite-pyrite-quartz vein. The geometry of both two veins indicates a sinistral movement. (F) The jamesonite-ferroan sphaleritepyrite-calcite vein crosscut the early stage of pyrite-quartz vein. (G–H) Cassiterite-pyrite-quartz vein were replaced by the jamesonite. The sample sampled from the ZK300-1 at −183 m from the Jianzhupo deposit. The photos and sample were provided by Shou-Yu Zhou. (I–J) The radial jamesonite coexisted with ferroan sphalerite and the jamesonite was replaced by the stibnite. (K) The reflected, BSE and CL images of cassiterite grain. Black holes, disorder CL image of the cassitertie and the jamesonite filled into the fractures of the cassiterite grain support the tin mineralization was later overprinted by the antimony mineralization. (L) Ferroan sphalerite drop-shaped inclusions could be found in the cassiterite grain under the reflected and transmitted light. Mineral abbreviations: Jam = jamesonite, Qz = quartz, Py = pyrite, Cal = calcite, Ma = marcasite, Stb = stibnite, Cst = cassiterite, Cp = chalcopyrite.

marcasite, pyrrhotite (*Po2*), and chalcopyrite (Fig. 9F, J–N). The pyrrhotite laths and lamelae (*Po2*), chalcopyrite blebs and stannite intergrew with *Sp1* to form a mosaic texture indicative of pyrrhotite-chalcopyrite-*Sp1*, chalcopyrite-*Sp1*, and stannite-*Sp1* solid solutions (Fig. 9H, K–M). Parts of stannite grew over *Sp1* as a thin rim and the *Sp1* is commonly enclosed by corase-grained enhedral *Py2* and enhedral arsenopyrite that in turn are surrounded by siderite vein (Fig. 9M). Minor cassiterite (*Cst1*) generally is anhedral and <40 μm and coexisted with *Sp1*.

The cassiterite (*Cst2*)-polymetallic sulfides of substage ii were formed in the middle of the cavities and replaced the sphalerite of substage i. The minerals are euhedral and dominated by cassiterite (*Cst2*), arsenopyrite, ferroan sphalerite (*Sp2*), pyrite (*Py3*), and euhedral siderite with minor quartz, fluorite, scheelite, and jamesonite (Fig. 9J). The euhedral-subhedral ferroan sphalerite (*Sp2*) inclusions with euhedral quartz and cassiterite replaced the coarse-grained ferroan sphalerite (*Sp1*) (Fig. 9L). Cassiterite (*Cst2*) was accompanied by arsenopyrite and quartz (Fig. 9J, L). The grains of the *Cst2* are generally 100–150 μm. Locally, some small inclusion of *Sp2* and *Py3* formed in the *Cst2*. Minor green and purple fluorite coexist with quartz. Minor subhedral disseminated (10–8 μm) scheelite formed in the erosion holes of the pyrite porphyroblasts (*Py1*).

The carbonate-sulfosalt-sulfide stage (substage iii) is characterized by extensive carbonate minerals (e.g. siderite with minor calcite and rhodochrosite) and minor euhedral-subhedral coarse-grained stibnite, low-Fe sphalerite (*Sp3*), galena, pyrargyrite, granular cassiterite (*Cst3*),

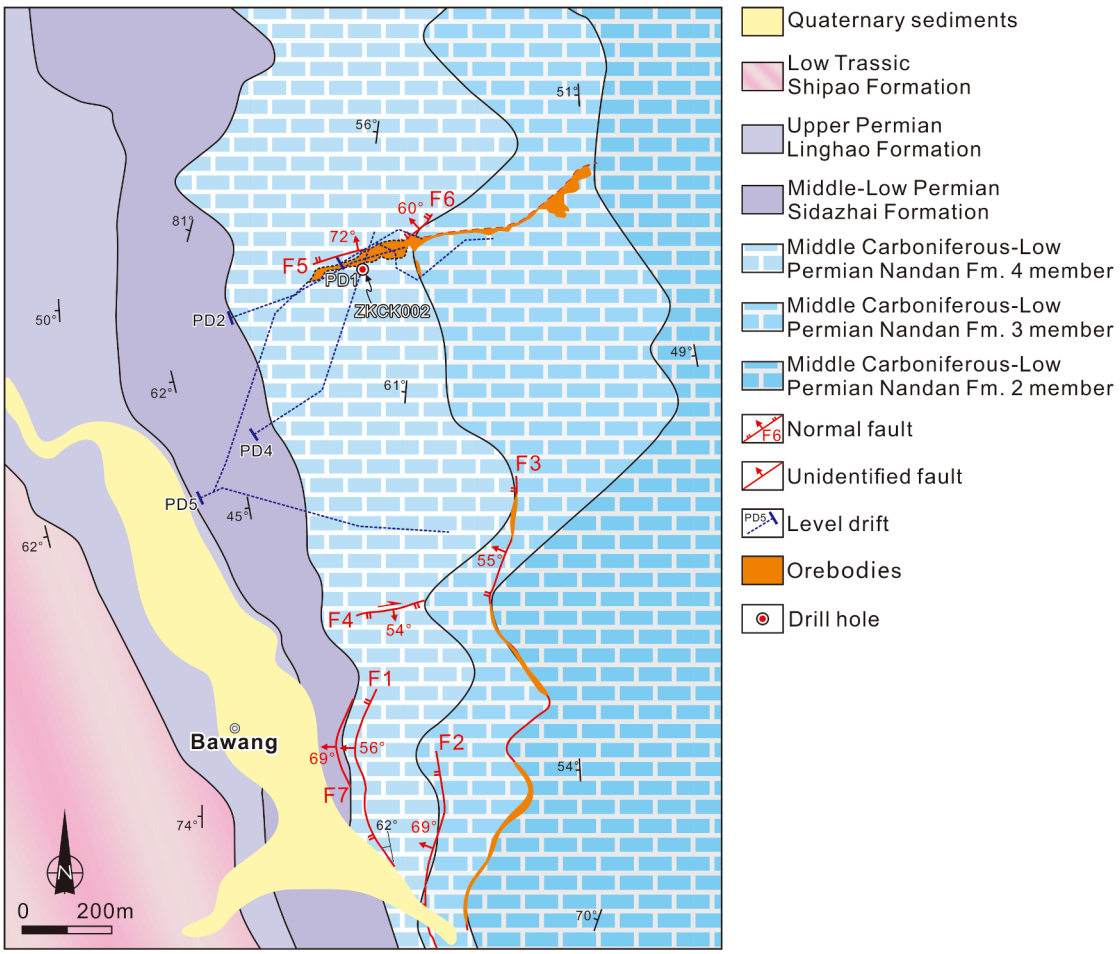

Fig. 6. Geological map of the Bawang Zn-Fe-Sn deposit and the distribution of orebodies (modified after SCSH, 2021).

and Bi-Pb-Ag-Sb-sulfosalt (e.g. kobellite, pavonite, galenobismutite). The cassiterite generally is euhedral-subhedral and 15–50 μm. The substage ii and iii are the main substages of ore formation in terms of both volume and economics. The supergene oxidation stage is characterized by the mixed ores which compose of limonite, pyrolusite, cuprite, and smithsonite. Relict rhodochrosite was replaced by pyrolusite (Fig. 9O). The limonite framboids generally formed along or around the rhodochrosite.

4. Methods and sampling

4.1. Methodology of structural analysis

The morphology of ore veins in natural exposures and mine workings was studied and their relations to geological structures established. The poles of strata and ore veins were plotted in stereographic projection. We also measured planes and linear structures (e.g., bedding, cleavage, vein bodies, ore zones, faults, jointing, slickenlines) and determined the slip sense from kinematic indicators (e.g., mineral steps, mineral fibers, fault grooves and fault mullions) in the field. Deformational kinematics and the paleo-orientation of stress were reconstructed in the Wuxu district using *FaultKin 8.1* and *Stereonet 10.0* software (Marrett and Allmendinger, 1990; Allmendinger et al., 2013; Cardozo and Allmendinger, 2013). Structural data were statistically analyzed and plotted on the upper hemisphere of the Wulff stereographic net using *Stereonet 10.0* software.

The detailed field study and local mapping were conducted in the Wuxu district during 2017 to 2020. This study revealed the particularities of the structures associated with the mineralization and establish the relationship with regional geodynamic events in the South China Block.

4.2. Mineralogical and textural date

A combination of hand specimen examination, polished sections and polished thin sections microscopy, and X-ray fluorescence spectrometer (XRF), and backscattered electron (BSE) microscopy has been used to generate a detailed paragenesis of the Jianzhupo and Bawang deposits. About 20 polished sections were examined using transmitted and reflected optical microscopes at the Laboratory of Dynamic Diagenesis and Metallogenesis, Institute of Geomechanics, Chinese Academy of Geological Science (LDDM-IGM, CAGS). Selected polished sections were examined using XRF and BSE on the ZEISS Sigma 300 high resolution field emission scanning electron microscopy (SEM) and JSM-6510A at the Key Laboratory of Paleomagnetism and Tectonic Reconstruction, Ministry of Natural Resources. Cassiterites had been observed carefully under the microscope and CL and BSE images were analyzed to characterize the texture of cassiterite and to avoid cracks and mineral/fluid inclusions.

4.3. LA-ICP-MS U-Pb dating of cassiterite

The size of cassiterites (5–20 μm) of sub-stages i and iii from the Bawang deposit are smaller than the spot size of the analytical laser. In this study, only cassiterite-quartz vein type ores (WX) of stage ii from the Jianzhupo deposit and cassiterite-ferroan sphalerite-quartz polymetallic sulfide type ores (BW1707) of substage ii from the Bawang deposit were selected for this study. Sample WX was collected from the ZK300-1 drill

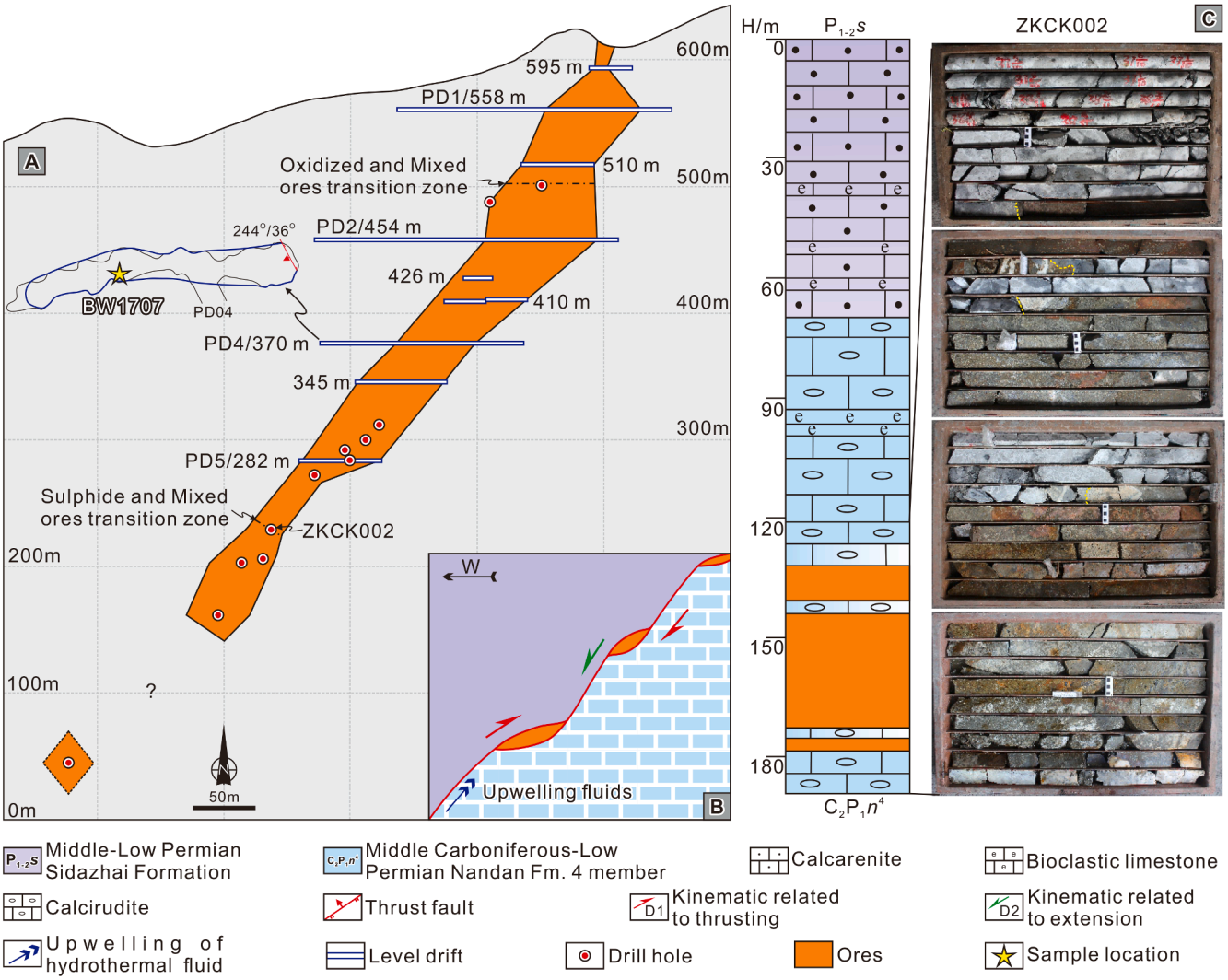

Fig. 7. (A) Cross section of No. I orebody from the Bawang deposit (modified after SCSH, 2021). (B) Schematic of the proposed mechanism for the ore-bearing cavities formed between the Middle Carboniferous-Low Permian Nandan Formation (C_2P_1n) and the Middle-Low Permian Sidazhai Formation ($P_{1-2}s$). The red arrow represent the kinematic relate to thrusting. The green arrow represent the kinematic relate to extension. The blue arrow represents the upward of the ore-forming fluid. (C) The photos of typical ores from ZKCK002.

core of the J130 orebody at −183 m from the Jianzhupo deposit (Fig. 3B). The thickness of J130 is 2.2 m with tin grade at 0.96 % (Liu et al., 2020a). Sample BW1707 was collected from the PD4 in the Bawang deposit (Fig. 7A). BW1707 is massive ore and consists of cassiterite, arsenopyrite, ferroan sphalerite, pyrite, and siderite with minor quartz.

Fully-dark zones or dark oscillatory zones of the cassiterite grains (Fig. 14), were analyzed for U-Pb ages and trace element concentrations using the Agilent 7900 Inductively Coupled Plasma Mass Spectrometer coupled to an Ar-F laser (LA-ICP-MS) at the Stake Key Laboratory of Ore Deposit Geochemistry, Institute of Geochemistry Chinese Academy of Sciences. Standard cassiterite AY-4 was used to determine U-Pb which yielded weighted mean $^{206}Pb/^{238}U$ age of 158.1 ± 1.6 Ma and ID-TIMS age of 158.2 ± 0.4 Ma (Yuan et al., 2008). The in-house cassiterite standard KA was used for quality control and obtained an age which is consistent with the age of ~ 430 Ma within error (Tang et al., 2020, 2021). The NIST reference glass SRM 612 was used to calibrate U, Th and Pb concentrations of cassiterite.

Cassiterite grains were analyzed using a laser energy density of 4 J/cm^2, a spot size of 44 μm and a repetition rate of 6 Hz. NIST SRM 612 and KA was analyzed twice and AY-4 was analyzed three times for every fifteen analyses of the unknown cassiterite samples. Each spot analysis incorporated a background signal acquisition of approximately 20 s followed by 35 s of sample data acquisition. Other conditions are listed by Tang et al. (2020, 2021). Raw data reduction was performed off-line by the ICPMSDataCal software. The uncertainty of the single population, ratio uncertainty of the AY-4 reference material, and decay constant uncertainties were propagated to the final results during the process of data reduction by ICPMSDataCal (Liu et al. 2008). Data errors for isotopic ratios in the cassiterite samples are 1σ. Isoplot 4.5 was used to calculate the U–Pb ages and draw Concordia diagrams (Ludwing, 2008).

5. Geometry and kinematic analysis of ore-controlling structures

5.1. Jianzhupo Zn-Sb polymetallic sulfide deposits

Two different Zn-Sb polymetallic mineralization geometries appear: a first mainly parallel subvertical mineralization consists of veins oriented NNW (345°) to NNE (5°) and consists of dm- to m-sized veins (Fig. 10). Poles of this type orebodies show a contoured maximum of 260°/14° (Fig. 10D). The second branching geometry mineralization is hosted in the two limbs, marked by cm stock veins and veinlets. The structures associated with the two types of ores in the Jianzhupo deposit

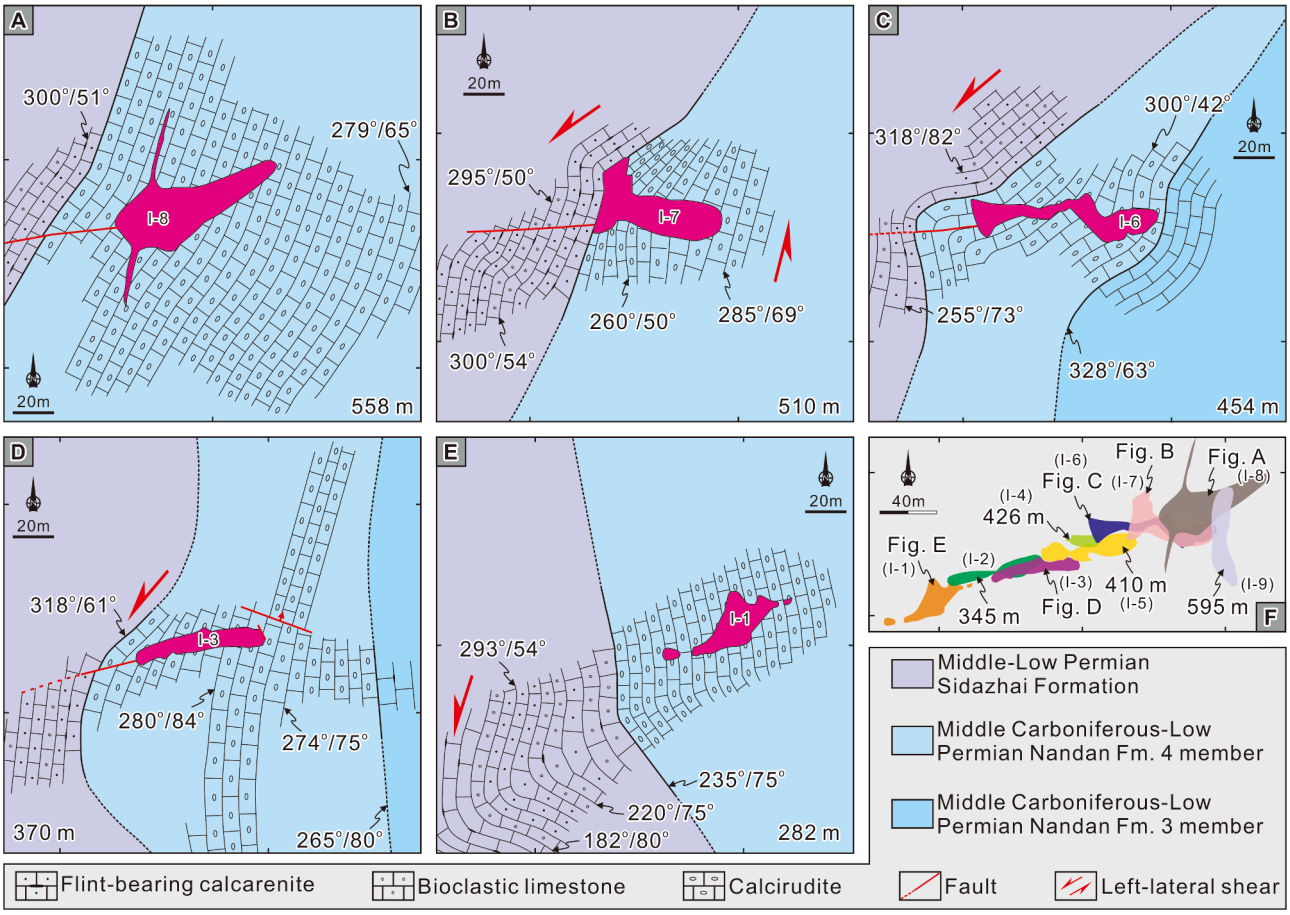

Fig. 8. Mining-level geological plan of different levels and kinematic analysis in the Bawang deposit (modified after SCSH, 2021). (A–E) Mining-level geological plan from 558 m to 282 m. (F) The projection of No. I orebody.

could divide into pre-, syn-, and post-mineralization structures as follows.

Pre-mineralization fold-and-thrust system. The structural architecture of Jianzhupo fold-and-thrust zone is characterized by a southwest-verging Jianzhupo anticlinorium and dextral strike-slip thrust faults that deform the Lower Devonian Tangding Formation (Figs. 2C, 3A, 4F–G). The geometries of the cleavage in both limbs of the anticline and interlayer crenulations document a compressional regime by a NE-SW orientated σ1. Parts of veins occupy axial-plane cleavages around the core of the Jianzhupo anticlinorium (Figs. 4A, 11A, B). The transverse joint sets (186°/82°, 101°/59°) developed on the limbs and oriented perpendicular to the fold axis (Fig. 4A, E), implying principal stress distributions of sub-horizontal SSW-trending σ1 (229°/17°), sub-vertical σ2 (109°/59°), and sub-horizontal NW-trending σ3 (327°/26°). Parts of these joint sets were infilled by the ferroan sphalerite-limonite-pyrite veins. The steeply dipping fractures and bedding-fractures are the main space for the stock veins in the surface (Fig. 4D–E). The main ore-bearing faults developed in the second member of the Low Devonian Tangding Formation (D_1t^2) in the west of the Jianzhupo anticline (Fig. 3A). These thrust faults dip 60°–80° to the NEE and bear minor oblique-slip striations that were overprinted by some dip-slip striations (Fig. 4F–H). Slip vector data from these faults imply these faults underwent dextral thrust and then sinistral normal fault. Though accurate chronological data of deformation are absence, an integration of our observation with previous data (Cai et al., 2004; Lepvrier et al., 2004; Li et al., 2019; Wu et al., 2019; Wang et al., 2021) promise us to infer these deformation in the Jianzhupo deposit belonging to D3. Most of these pre-ore structures were reused in the *syn*-mineralization stage by the evidence that slickenside surfaces can be marked by sets of slickenlines of two (or more) different orientations.

Syn-mineralization extension-sinistral strike-slip faulting. Since kinematic indicators (such as slickenlines, mineral steps, mineral fibers) are difficult to save, the kinematics of *syn*-mineralization structures are not obvious in the Jianzhupo deposit. Slip vector data and mineral fibers on the pre-existing NNW-striking fault planes illustrate a near E–W extension during this deformation (Fig. 4F, H). Some disseminated sphalerite, galena, and stibnite are found in these fault zones. Kinematically, the limbs of the Jianzhupo anticline are deformed by several asymmetric folds with subhorizontal axial planes and imply normal shear (Figs. 9A, 11E–G, 12). Cross-section views of the geometries of the dilational rhombs that form in the proximal parts of sub-parallel cleavages imply a component of top to the down shear (Fig. 11A–D).

Map view of the geometries of the ore-bearing NNW-striking faults and main stage orebodies within the first order faults show a top-to-the north sense of shear (Figs. 3A and 10). The second and third order mineralized rhombs and pull-apart zones are filled with sphalerite, jamesonite, stibnite, manganocalcite, and calcite (Figs. 10A, C, E–F, 11A–D). Generally, the main orebodies are controlled by the first order faults and the high grade ore-shoots form in small dilational spaces controlled by the second and third order fractures. Geometry of ore-shoots between the sub-parallel main orebodies can be interpreted as a pull-apart opened in a sinistral top to the north movement and controlled by NNW-striking faults and cleavages (Fig. 10E–D). The geometries of the quartz-sphalerite-pyrite vein from stage ii and the stibnite-calcite vein from stage iii suggest that the sinistral shear was persistent during the ore-forming process (Fig. 5D–E). Cassiterite grains exhibit jigsaw geometry infilled by jamesonite that illustrate antimony mineralization overprinting tin mineralization (Fig. 5K).

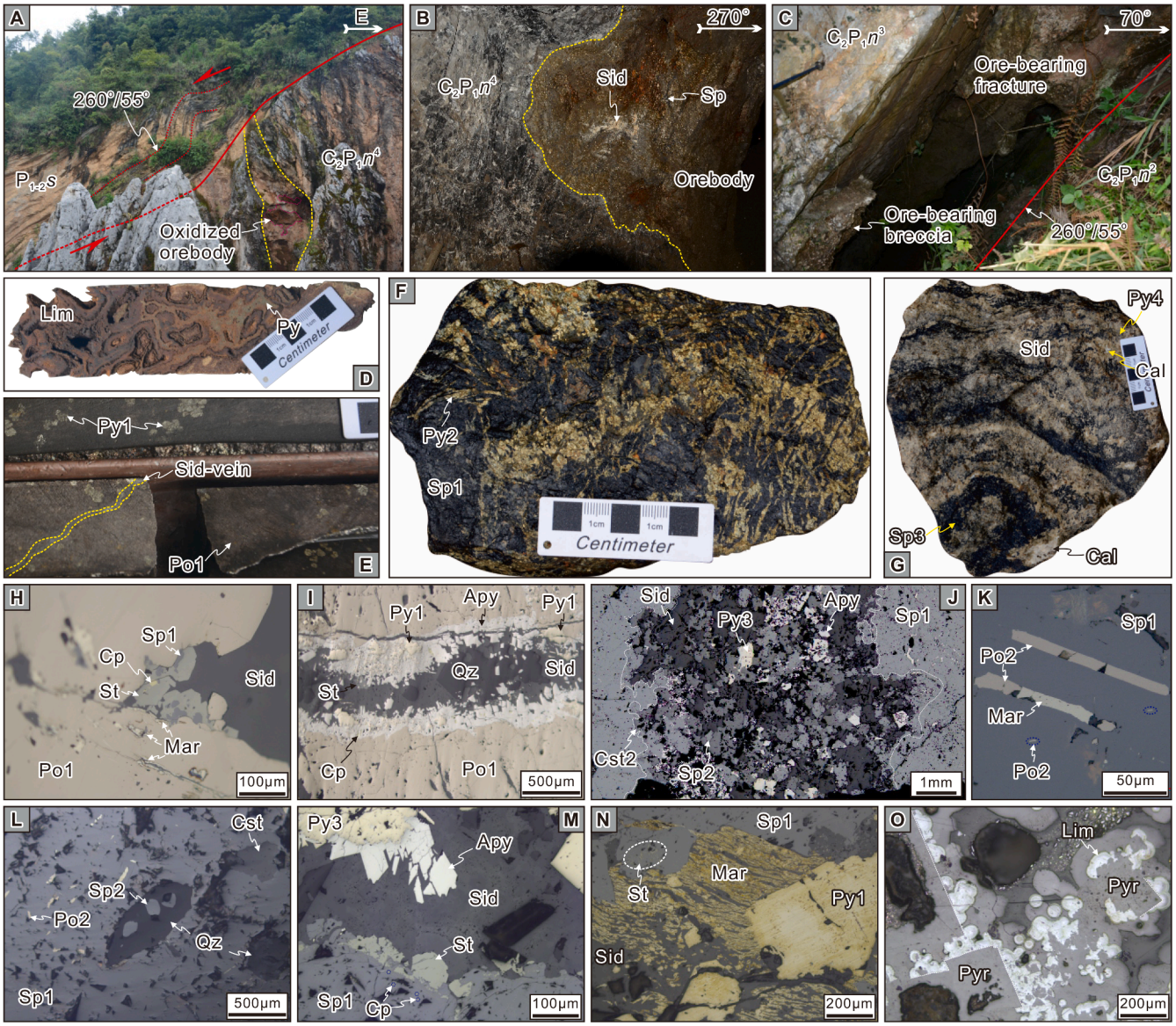

Fig. 9. Orebodies and minerals of the Bawang deposit. (A–B) No. I orebody formed in the cavities in the Nandan formation calcirudyte. (C) NS-striking orebody formed in the bedding-fracture. (D) Mixed ores in the surface. The ores compose of limonite and pyrite. (E) Massive pyrrhotite was cut by the siderite vein. The euhedral pyrite porpyroblasts grew in the massive pyrrhotite implies a annealing process. (F) Massive ferroan sphalerite-pyrite-sphalerite ore of substage i. (G) Banded ferroan sphalerite-siderite ore from substage iii. The ore is replaced by the calcite-pyrite veins. (H–I) The massive pyrrhotite was replaced and crosscut by the ferroan sphalerite-stannite-chalcopyrite-arsenopyrite-quartz-siderite vein. Black dissolution pores developed on the surface of the pyrrhotite. (J) Euhedral cassiterite + sphalerite + arsenopyrite + pyrite + siderite vein of substage ii crosscut and replaced the massive sphalerite of substage i. (K) The pyrrhotite laths and lamelae intergrew with sphalerite of substage i to form a mosaic texture. (L) Euhedral quartz + sphalerite vein of substage ii replaced the sphalerite of substage i. (M) Euhedral arsenopyrite + siderite vein replaced the pyrite + sphalerite + stannite. (N) Siderite replaced pyrite, stannite. The marcasite formed by the siderite replaced pyrite. (O) The mixed ores compose of limonite, and pyrolusite. The rhodochrosite change into pyrolusite and kept the crystal shape of rhodochrosite. The limonite framboids generally formed along or around the rhodochrosite. Mineral abbreviations: Lim = limonite, Sid = siderite, Po = pyrrhotite, St = stannite, Mar = marcasite, Apy = arsenopyrite, Pyr = pyrolusite.

Post-mineralization faulting. The EW-striking, south steeply-dipping faults are the youngest structural features encountered in the Jianzhupo deposit. These faults displaced main stage veins and the pre-existing NW-, and NE-striking faults (Fig. 13). These faults lack alteration or contain up to 3 cm thick of white/grey calcite and yellow clay gouge. The displaced marker units indicate orthogonal reverse-dextral displacements of up to 5–20 cm on these structures (Fig. 13).

5.2. *Bawang paleokarst infilled type Zn-Fe-Sn polymetallic deposits*

Inadequate outcrops and the development of steep cliffs have made kinematic analysis of structures at Bawang difficult. The level drifts and drill holes show that the paleokarst are the main ore-bearing structures. Two types of cavities appear: a first mainly "stepped" geometry mineralization is hosted in the EW-trending cavities. The second are limestone breccia ores cemented by limonite and calcite located within interbedding fractures (Figs. 6 and 9C). Two distinct events are suggested by the two types of ore.

The earliest event is accompanied with the formation of the Wuxu anticlinorium under the NE–SW orientated compression. The geometries of the ore-bearing cavities from 558 m to 282 m could be explained by the bedding-shear in the west limbs during the Wuxu anticlinorium development (Figs. 7 and 8). Owing to the competency difference, the E–W-striking dilation could form between the thick-bedded calcirudytes

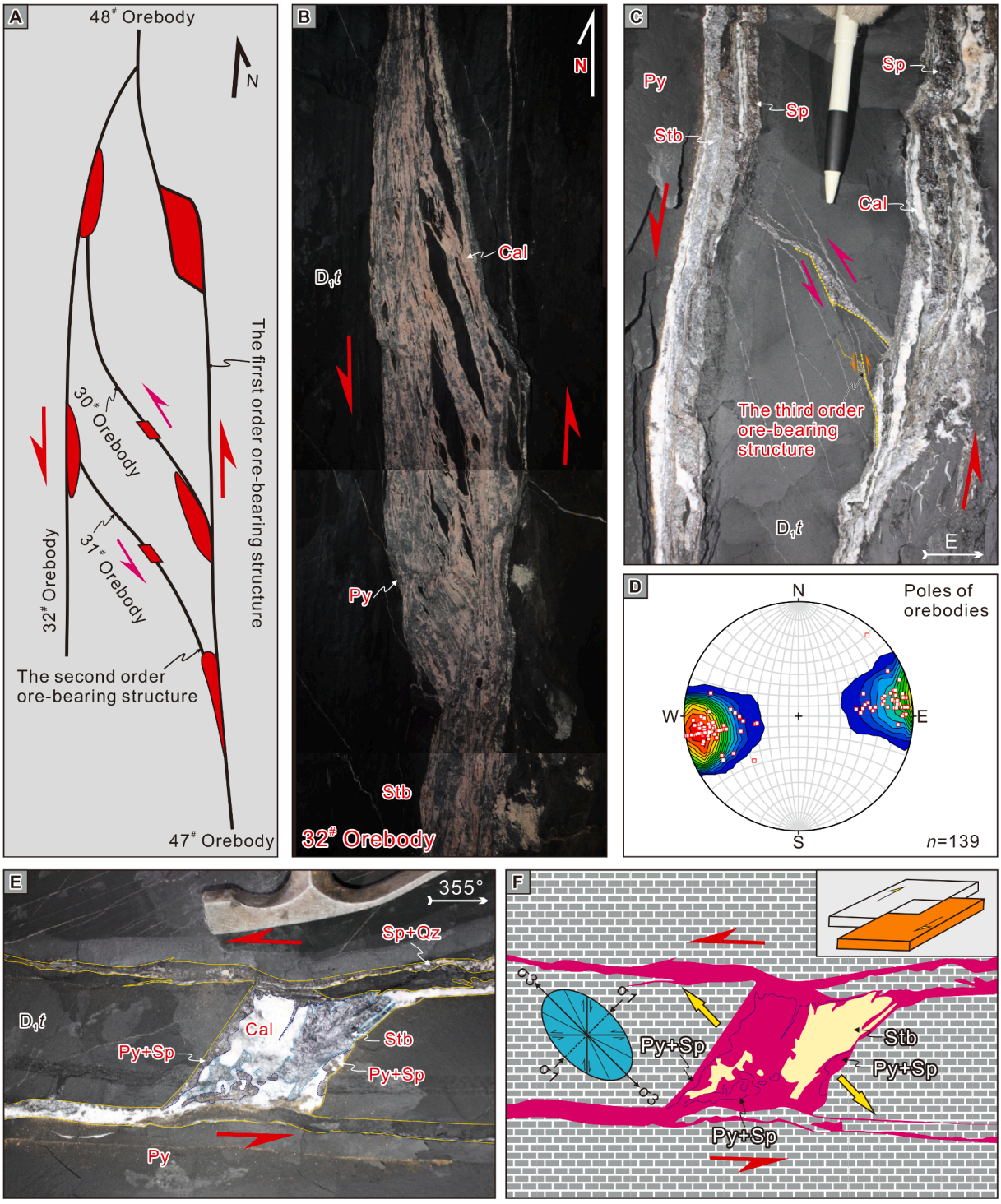

Fig. 10. The characteristic of ore control structures in the Jianzhupo deposit. (A) Schematic of structural ore-controlling style for the NS-striking main orebodies in the Jianzhupo deposit. The ore-shoots filled in the rhomboidal spaces along the striking or in the junction of the main and secondary faults. (B) Big dilational rhombs in Tangding Formation (D_1t) filled with ore-shoots which consist of calcite, stibnite, ferroan sphalerite, and pyrite. (C) Multiple order structure control ores of No.7 orebody. (D) Stereonets (lower hemishere, equal angle) of poles to the orebodies in the Jianzhupo deposit. (E–F) Small pull-apart along the NNW-trending structures in the Tangding Formation (D_1t), creating rhomboids filled with ferroan sphalerite, stibnite, pyrite, and calcite. The geometry of the pull-apart implies a sinistral movement. The red, magenta, and green arrow represent the kinematic relate to the 1th, 2th, and 3th order ore-bearing structures.

($C_2P_1n^4$) and flint-bearing calcarenite ($P_{1\text{-}2}s$) during the bedding-shear (Fig. 7B). The geometry of orebody II demonstrates that inter-bedding fractures form between the siliceous rocks and crystalline limestone (Fig. 9C). The breccia ores suggest a characteristic of epigenetic accumulation. The steeply dipping bedding planes are the favorable planar breaks that serve as the principal structural guides for meteoric waters in karstified rocks in the Bawang deposit. Dubljansky and Kiknadze (1983) pointed out that bedding planes or contacts are more favorable than joints or faults for forming cavities. Therefore, the ore-bearing cavities may be belonging to the pre-mineralization structures.

The geometries of the crenulations of Sidazhai Formation flint-bearing calcarenite indicate normal shear (Fig. 9A). Mining-level

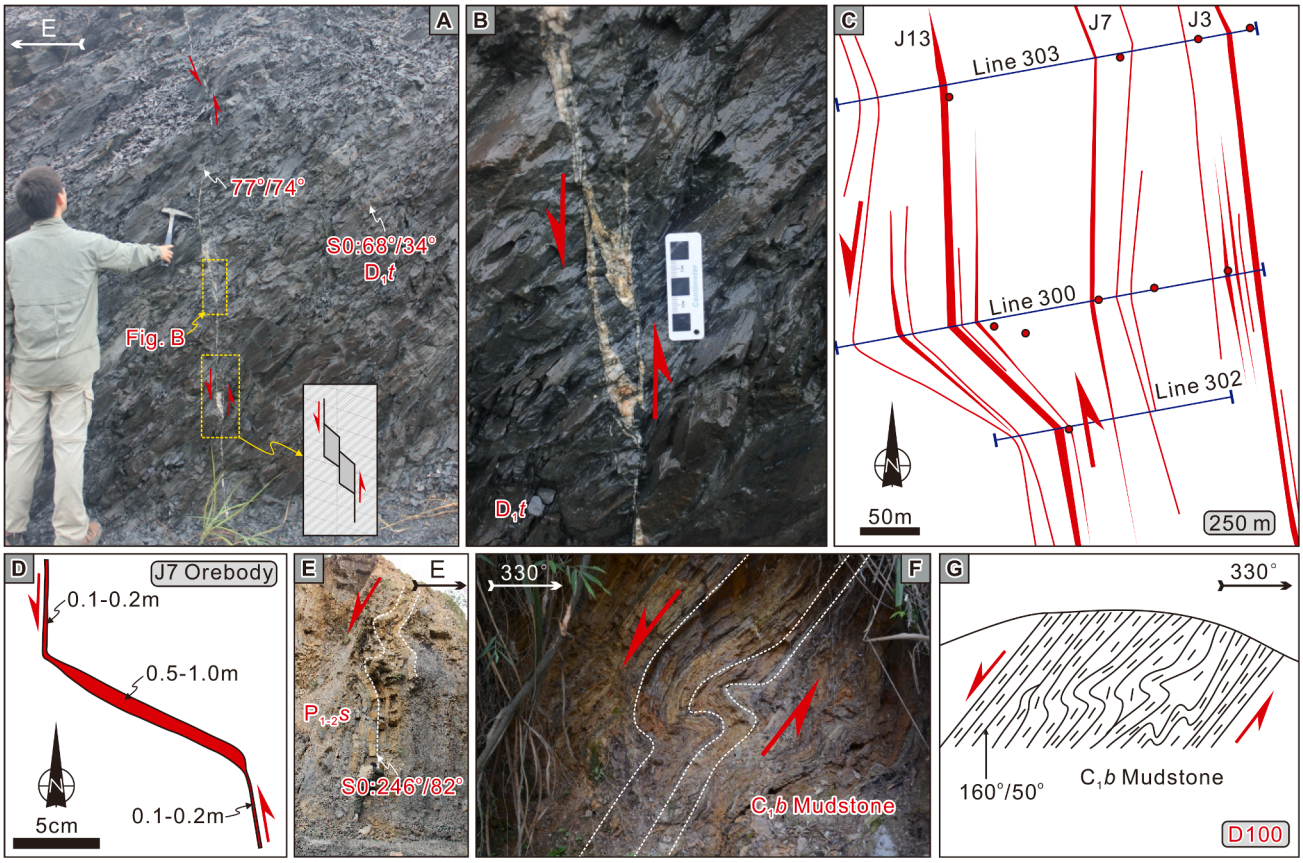

Fig. 11. The characteristic of structures forming during the mineralization in the Jianzhupo deposit. (A–B) Steeply-dipping quartz vein formed in the Tangding Formation. The rhomboids indicate a top-to-down movement. (C–D) Geometry of the orebodies in the mining-level geological plan at 250 m and J7 orebody imply a sinistral and top-to-down movement. The blue lines represent the prospecting profiles. (E–G) Asymmetric folds with subhorizontal axial planes in the Baping and Sidazhai Formation imply normal shear.

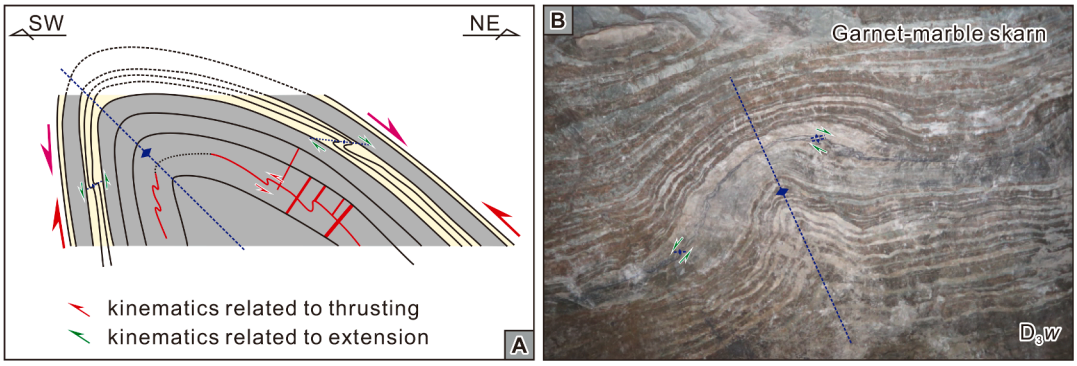

Fig. 12. (A) Schematic of the proposed mechanism of two phase deformations in the Wuxu district. (B) Outcrop picture of the two phase deformations in the Wuzhishan Formation (D_3w) from the Dachang district, middle of the Danchi belt.

geological plans of different levels imply a component of top to the northeast and down to the southwest shear (Fig. 8). The geological map and mining-level geological plan of different levels in the Bawang deposit display that the EW-striking faults are parallel to the ores. Underground observations display that some small dilational spaces along the EW-striking fracture filled with sphalerite and pyrite. It indicates that the EW-striking faults maybe the passageway for the ore fluids. The geometries of the orebodies in the 595 and 558 levels imply the NS-striking inter-bedding faults also the passageway for the ore fluids.

6. U-Pb age of cassiterite in the Wuxu district

6.1. Cassiterite CL and BSE textures

Most of the cassiterite grains from Wuxu district show euhedral crystal shapes. Most grains are prismatic with aspect ratios of 1:1–1:3, lengths 100–300 μm, and are opaque and light yellow under an optical microscope from the Bawang deposit. Both elbow and penetration twins in cassiterite were widely observed (Fig. 14A–B). CL intensity of cassiterite from the Bawang deposit is much higher and is typically bright in CL images with very obviously oscillatory zones parallel to the growth direction. Half of the cassiterite grains underwent late

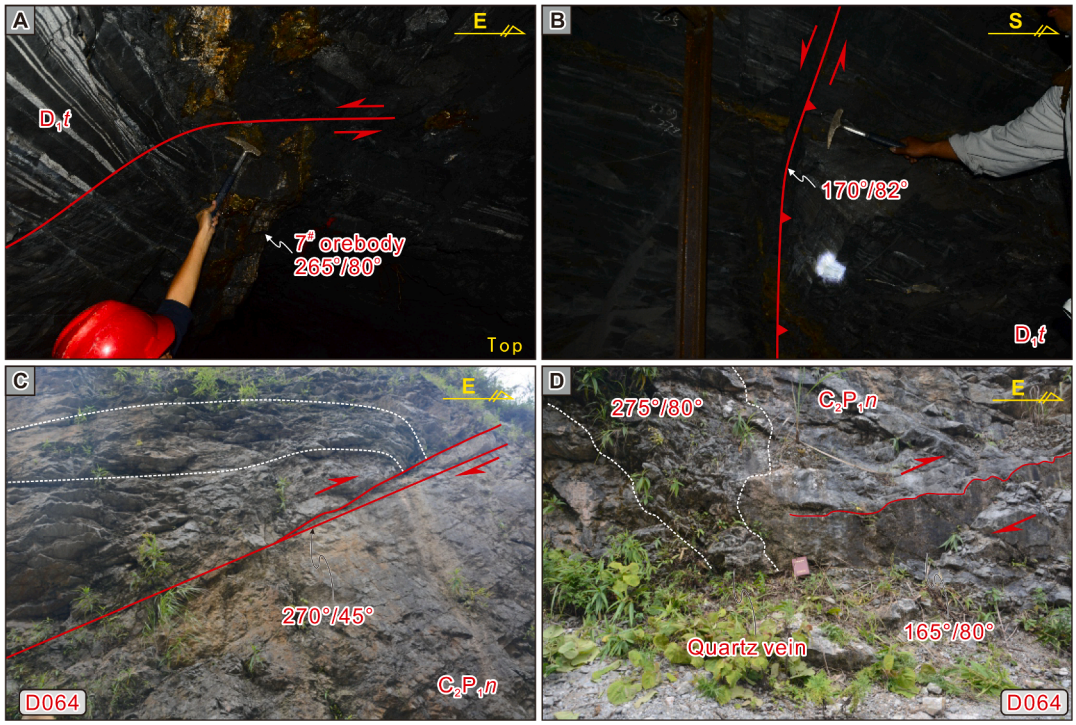

Fig. 13. The characteristic of post-mineralization structures in the Wuxu district. (A–B) The EW-striking dextral thrust fault cut the J7 orebody in the Jianzhupo deposit. (C–D) The EW-striking dextral fault cut the NS-striking quartz vein at geological observation point D064.

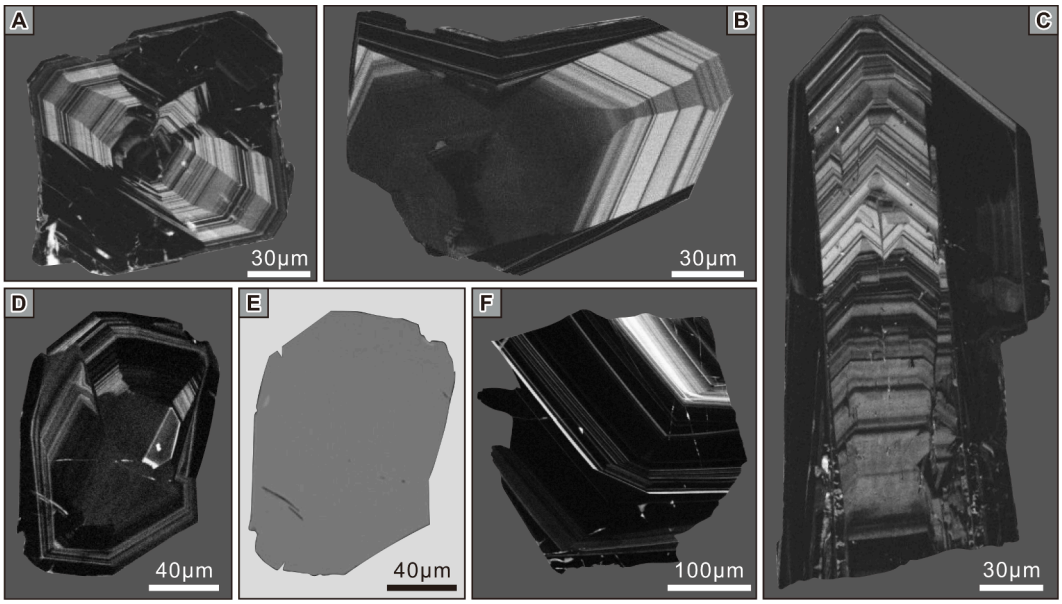

Fig. 14. Cathodoluminescence and back-scattered electron images of representative cassiterite samples analyzed by laser ablation–inductively coupled plasma–mass spectrometry (LA-ICP-MS). (A–C) Sample BW1701 from Bawang deposit with distinct oscillatory zoning. Both elbow and penetration twins in cassiterite were widely occurrence. (D–F) Sample WX from Jianzhupo deposit with distinct oscillatory zoning cut by white late-stage veinlets.

hydrothermal alteration which is characteristic of the pleochroic, pore-rich lighter zones.

The cassiterite grains are prismatic with aspect ratios of 1:1–1:2, have lengths 100–500 μm, and are translucent and primrose yellow to brown under an optical microscope from the Jianzhupo deposit (Fig. 5L). Crystal twinning of cassiterite is not common in the Jianzhupo deposit. CL intensity of cassiterite from the Jianzhupo deposit is relatively lower than the cassiterite grains from the Bawang deposit (Fig. 14D–F). Most of the cassiterite grains were broken. The hydrothermal alteration of the cassiterite grains is relatively weaker than the cassiterite grains from the Bawang deposit.

6.2. Cassiterite U-Pb age

The analytical results of U–Pb isotopes of the cassiterite samples from Wuxu district are listed in ESM Table 1 and illustrated in Fig. 15. The grains have a relatively high common Pb contents from 0.6 ppm to 10 ppm, low Th contents of < 0.4 ppm (0.03 ppm average) and U contents

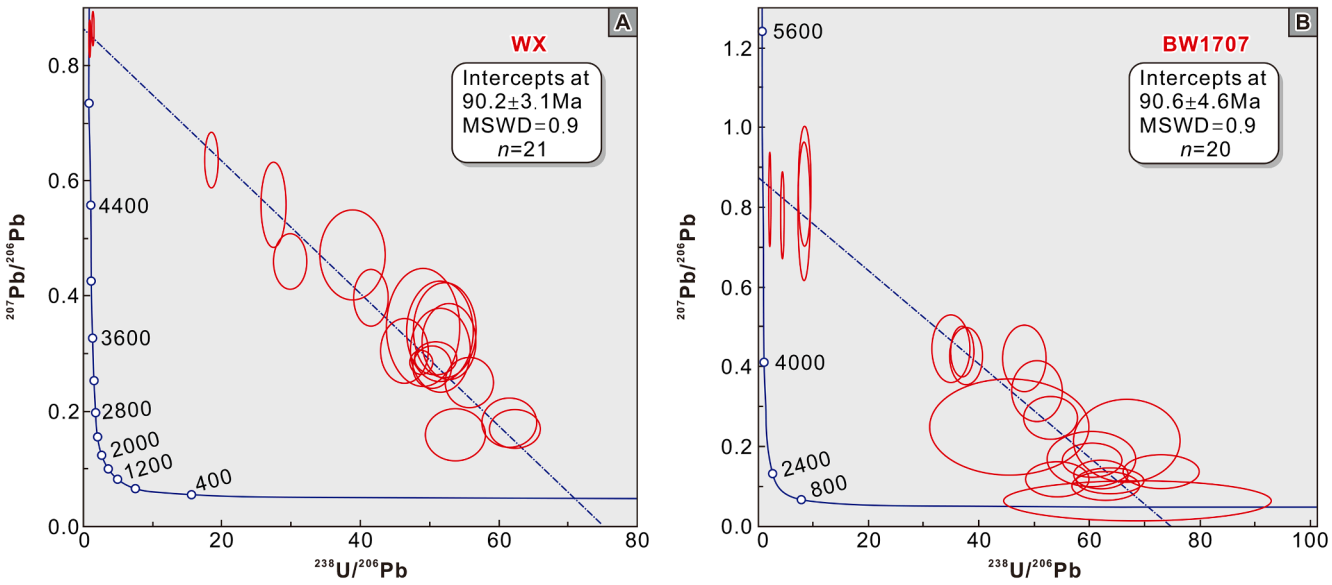

Fig. 15. Lower intercept Tera-Wasserburg U-Pb Concordia age diagram for cassiterite from the Jianzhupo (A) and Bawang deposit (B), respectively.

varying from 0.76 to 8.96 ppm (<10 ppm average). Owing to the relatively high common Pb in cassiterite, the lower intercept Tera-Wasserburg U-Pb Concordia age is used. Twenty-one spots yielded a lower intercept value of 90.2 ± 3.1 Ma (1σ; MSWD = 0.9; n = 21) in the Jianzhupo deposit. Twenty spots yielded a lower intercept value of 90.6 ± 4.6 Ma (1σ; MSWD = 0.9; n = 20) in the Bawang deposit.

7. Discussion

7.1. Time of tin mineralization in the Wuxu Zn-Sb-polymetallic district

Until now, there was no radioisotopic data to constrain the timing of the mineralization in the Wuxu district. In this study, ore mineralogy shows the jamesonite and stibnite is later than the cassiterite in the Wuxu district. The metallogenic evolution is similar to the Dachang district (Cai et al., 2007). The lower intercept of the cassiterite U-Pb age in the Tera-Wasserburg concordia indicates that the tin-zinc mineralization in the Jianzhupo and Bawang deposits occurred around 90.2 ± 3.1 Ma and 90.6 ± 4.6 Ma, respectively. It means that the tin mineralization occurred during 91–90 Ma.

In the Danchi fold-and-thrust belt, the emplacement depths of the felsic intrusions increased from north to south (Fig. 2A; Fu et al., 1993). LA-ICP-MS zircon U-Pb dating of porphyry granite dykes yielded ages of 89.1 ± 0.9 Ma from the Mangchang district (Wu et al., 2020). The SHRIMP zircon U-Pb age of quartz diorite porphyrite and granitic porphyry dikes yielded ages of 91 ± 1 Ma and 91 ± 1 Ma from the west of Dachang district, respectively (Cai et al., 2006). The LA-ICP-MS/SHRIMP zircon U-Pb age of Longxianggai pluton yielded ages of 99–88 Ma in the middle of the Dachang district (Cai et al., 2006; Liang et al., 2011; Li et al., 2008; Xiao, 2018; Huang et al., 2019; Wang et al., 2019). Guo et al. (2021) defined biotite granites related with tin mineralization and the post-ore granite porphyry dykes were emplaced at 93 Ma and 86 Ma, respectively. All of these data represent the timing of felsic intrusions in the Danchi belt. As mentioned above, three types of deposit in the Danchi belt. Until now, most of the mineralization ages conducted only in the Dachang district. Tin mineralization age of Dachang district was defined by quartz Rb-Sr ages of 98.6 – 93.4 Ma (Wang et al., 2004; Cai et al., 2005, 2006; Li et al., 2008), garnet Sm-Nd age of 95 Ma (Liang et al., 2011), muscovite and sanidine ^{40}Ar-^{39}Ar ages of 93.5 –91.4 Ma (Wang et al., 2004; Xiao, 2018), molybdenite re-Os isochron age of 91.6 Ma (Xiao, 2018), sphalerite Rb-Sr ages of 106–94 Ma (Zhao, 2003), and cassiterite U-Pb of 95.8–91.2 Ma (Wang et al., 2015; Guo et al., 2018).

Our first dating results for the tin-polymetallic mineralization in the Wuxu district have a close temporal link with these in the Dachang and Mangchang districts. Gravity data and CSAMT sounding works also support that the concealed felsic intrusions existed in the Wuxu district (Fig. 1B; Zhao et al., 2020). Hence, we conclude that Wuxu district have a great potential for tin mineralization associated the concealed intrusions.

7.2. Overall structural controls on mineralization at the Wuxu district

Ore-bearing veins in the Wuxu district record at least two tectonic events associated with regional deformation (D3 and D6) based upon faulting and fold orientations (Figs. 4A, 12). Three major types of mineralization have a strong relationship with these two deformational stages.

During the NE-SW shortening deformation, the NW-striking fold-and-thrust system formed. In the core of the Wuxu anticlinorium, the sub-parallel axial-plane fractures developed and provided space for the ore-forming fluids in the Jianzhupo deposit. Syn-deformation transverse joint sets and bedding-fractures developed in the whole district, providing space for the veinlets and branching veins in the Jianzhupo deposit and for the No. II orebody in the Bawang deposit. During this process, bedding-shear could lead to form some “stepped” geometry dilational zones at the contact between the Nandan Formation calcirudytes and the Sidazhai Formation flint-bearing calcarenite and bioclastic limestone.

Cavity formation is often easier at the contact between limestone and clastic rocks (Dubljansky and Kiknadze, 1983). Therefore, this maybe a reasonable explanation for the paleokarst cavities formation between the steeply dipping Nandan Formation limestone and Sidazhai Formation sandstone and siliceous rocks. The steeply dipping bedding planes were the effective fluid flow paths for meteoric and river waters and lead to dilational zones and formation of cavities which is favorable spaces for the paleokarst infilled type ores in the western of Wuxu district.

During the E–W extensional deformation, the dilational rhombs or jogs developed along strikes and dips when the pre-existing NW-striking faults reactivated preexisting anisotropies. Ore mineralogy shows mineral infilling during the progressive produced dilational zone which is associated with the high grade ore-shoots, such as the No. 7 orebody and the orebodies in the 250 levels from the Jianzhupo deposit (Fig. 11C–D) and No. I orebodies from the Bawang deposit (Figs. 6 and 9C). All of the

geometries of the high grade ore-shoots suggest a sinistral top-to-the north sense of shear. This stage of deformation is common in the north of the Danchi fold-and-thrust belt, such as Dachang district (Cai et al., 2004; Xiao, 2018; Wu et al., 2019). Cai et al. (2014) found that felsic dikes, Zn-Cu orebodies, and fluorite-scheelite veins all formed in the NS-striking fracture zone. Surrounding rocks on both sides of the NS-striking faults formed skarn. The idiomorphic and coarse arsenopyrite, pyrites, and sphalerite in the NS-striking fractures imply an open-infilling characteristic or replacement which is common for skarn formation. (Fig. 16). Previous studies show that magma emplacement, the opening of the NS-striking fractures, and sulfides growth were synchronous in the north of the Danchi belt (Fig. 17; Xiao, 2018). The direction of the *syn*-mineralization magma emplacement was from SW to NE which is similar to the direction of the fluid migration of the Bawang deposit that is supported by the mineral assemblage from erroan sphalerite masses (*Sp1*) with minor pyrrhotite laths, chalcopyrite blebs, stannite (below 200 m) to cassiterite + pyrite + siderite + arsenopyrite + sphalerite with minor scheelite-quartz-fluorite minerals (200 to 500 m) to calcite + stibnite + Bi-Pb-Ag-Sb sulfate to limonite (350 to 600 m) (Fig. 7B; Fu et al., 1993; Guo et al., 2018). The euhedral pyrite porphyroblasts (*Py1*) formed in the massive pyrrhotite imply reequilibration of the pyrite and pyrrhotite from the substage i in the Bawang deposit occurred during cooling at temperatures above 300 °C (Fig. 9E; Brooker et al., 1987; Craig et al., 1993). Generally, the annealing phenomenon of pyrrhotite is obvious when the centigrade is up to 450 °C (Marshall and Gilligan, 1987). Experimental testing of chalcopyrite disease of sphalerite implies a result of diffusion at 400–700 °C (Bente and Doering, 1993). According to iron and zinc partitioning between stannite and coexisting sphalerite, the stannite-sphalerite pair form from 250 °C to 450 °C (Shimizu and Shikazono, 1985; Nagashima et al., 2016). The common development of the exsolution textures composed of pyrrhotite, chalcopyrite, stannite with ferroan sphalerite and three sulfides together (stannite, chalcopyrite, ferroan sphalerite) in the Bawang deposit during the substage i also imply a middle-high temperature zinc polymetallic mineralization which is earlier than Sn-, and Sb-polymetallic mineralization. Spectrum data display that the iron contents of sphalerite from the Zn-, Sn-, and Sb-polymetallic mineralization vary from 12 to 15 %, 11–13 %, and 2–4 %, respectively. Previous studies have shown that iron contents of sphalerite have a positive correlation between the temperatures of hydrothermal fluids (Scott and Barnes, 1971; Scott, 1983; Keith et al., 2014). Therefore, the vertical zonation of the Sb-, Sn-, and Zn-polymetallic mineralization is also accompanied with the increasing of temperature of hydrothermal fluids from shallow to deep.

Generally, the common geometry suggests that the Wuxu district formed during the formation of the NE-SW fold-and-thrust systems, following EW-directed extension. The middle-high temperature ore-forming fluids filled into the structures which during this two stages deformation. The vertical zonation of mineralization in Wuxu district controls by the ore-bearing structures and the temperature of hydrothermal fluids. In the single cavities, sulfur fugacity and temperature may control the ore horizontal zonation.

7.3. Implications and prospecting significances

Up to 90 % tin metal occur in magmatic-hydrothermal type ores that contribute a significant part to the total tin resources in the world (Mao et al., 2019). In the magmatic-hydrothermal systems, cassiterite-sulfide ores can occur in both proximal (such as porphyry, greisen, and skarn type deposit which adjacent to the granitic pluton) and distal (such as hydrothermal replacement and infilling type magmatic-hydrothermal deposit which generally far from the granitic pluton) ore deposits (Kwak, 1987). Often, the distal replacement and infilling type deposits are some of the large or giant tin deposit, such as Renison Bell deposit in the Australia (Patterson et al., 1981) and the Gejiu ore district in the southwestern of the Youjiang Basin, China (Cheng et al., 2013; Guo et al., 2018; Mao et al., 2019; Liu et al., 2020b). Different from proximal magmatic-hydrothermal deposits that was directly controlled by around granites, tin-polymetallic orebodies in the distal magmatic-hydrothermal deposits are major branching geometry that controlled by the steeply-dipping faults and adjacent bedding-fractures (Kwak, 1987).

The genesis of these tin deposits has been debated for decades in the Danchi fold-and-thrust belt (Han et al., 1997; Cai et al., 2007; Guo et al., 2018; Zhao et al., 2021). The key issue is that all of the orebodies (especially the stratiform orebodies, such as No. 91 and 92 orebodies) are controlled by the Devonian strata in the Dachang district. Since the paleokarst infilled type and stratiform orebodies were found between the Carboniferous and Permian in the Bawang and Sanpaidong deposit, we conclude that the Devonian strata are not the key factor for the ore formation. It also means that the bedding-fractures, formed in the pre-mineralization fold-and-thrust system under the NE-SW shorting deformation, are all potential ore-bearing structures in the Danchi fold-and-thrust belt. The orebodies in the Jianzhupo deposit of Wuxu district were hosted in the Devonian strata, but most orebodies are comprised of steeply-dipping veins. The total $\delta^{34}S_{\Sigma S\text{-fluids}}$ value of the ore-forming fluid is 5.93 ‰ which was calculated by the $\delta^{34}S_{VCDT}$ values of sphalerite and coexisting pyrite from the Jianzhupo deposit (Liu et al., 2020a). The peak value of $\delta^{34}S$ (-8‰ to + 4 ‰) from the vein-type ores is close to that of the stratiform and massive ores in the Dachang district (Zhao, 2003). These sulfur isotope compositions also suggest the sulfur was predominatly derived from magmatic source. In the light of the structural control, cassiterite chronology, and ore mineralogy, combing the sulfur isotope compositions from predecessors' studies, tin

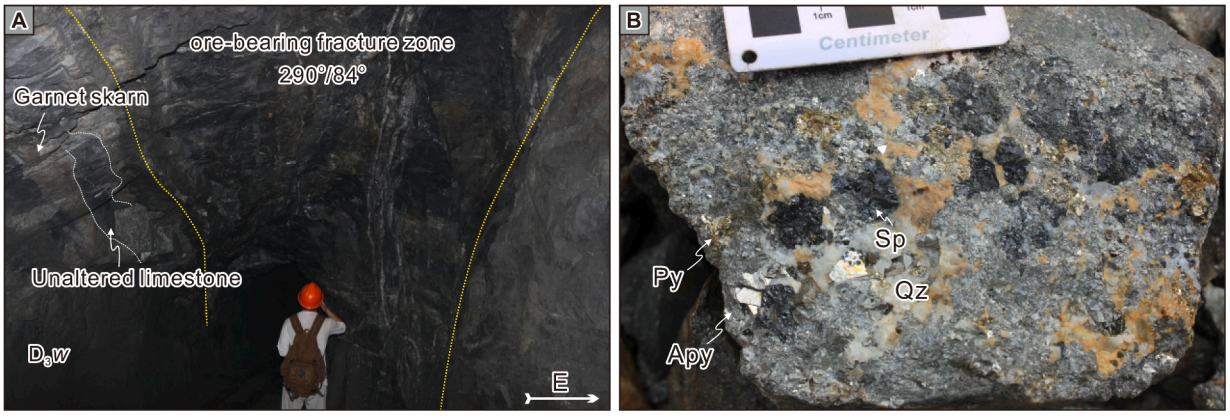

Fig. 16. (A) The NS-striking ore-bearing fault in the Lama deposit, Dachang district, middle of the Danchi belt. (B) Ores in the NS-striking fault which consist of coarse, euhedral arsenopyrite, ferroan sphalerite, pyrite, quartz.

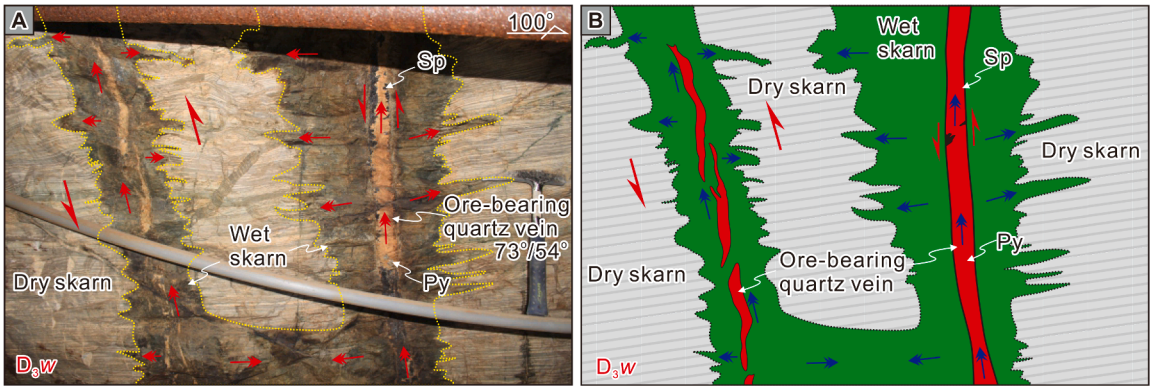

Fig. 17. The near-NS-striking sub-vertical ferroan sphalerite-quartz vein and branching geometry wet skarn (epidote-dominated skarn) overprinted on the dry skarn (garnet-marble skarn) in the Lame deposit, Dachang district, middle of the Danchi belt. The growth orientation of the ferroan sphalerite implies sinistral movement (down-to-top) and horizontal bedding shear during the mineralization.

mineralization in the Wuxu district is associated with magmatic rocks rather than submarine exhalations during Devonian.

The paleokarst infilled tin-sulfide ores are one of particular type ores in the distal hydrothermal tin-polymetallic deposit, owing to the cavities in the karst regions are the most ideal space for the ore-forming fluids (Smith et al., 2013). The ore-bearing cavities formed in the west of Wuxu anticlinorium attributing to two factors. The first factor is contrasting deformation behaviors between ductile thin limestone and mudstone versus brittle more competent massive-thick calcirudite. During the NE-SW shorting deformation, the dilational zones easily formed in the brittle more competent calcirudite. The second factor is steeply-dipping bedding planes which formed in the west of Wuxu asymmetric anticlinorium. The downward meteoric and river waters along the steeply-dipping bedding planes between the Nandan and Sidazhai Formations led the pre-existing dilational zones to form and enlarge dissolution cavitis. Hence, we speculate that the western of the Dachang anticline have a great potential for paleokarst infilled type ores. This may be one of reasonable explanations why No. 100 orebody with a curved shape and why a single orebody contains huge amount of metal.

8. Conclusions

(1) The geometry of ores in the Wuxu district are typical example of structurally controlled mineralization characterized by the overprinting of multiphase tectonism, from NE-SW shortening to E–W extension and E–W shortening. The NE-SW shortening deformation controlled the structural framework of Wuxu district. This multiphase deformation is expressed by NW-verging thrusts and folds, axial-plane cleavages around the core of the Wuxu anticline, transverse joint sets on the limbs of the Wuxu anticline, and dilational zones in the bedding-fractures. Afterward, an E–W extension stress field produced new formed NS-striking normal faults and reactivated pre-existing NNW-striking faults which expressed by sinistral top-to-the north sense of shear. During this deformation, some more low order dilational spaces of the NW-striking faults and bedding-fractures formed and a *syn*-kinematic deposition of minerals in these hosting structures. The post-mineralization EW-striking faults is not obvious and displaced preceding two phase structures and ores.

(2) Mineralogical studies have shown that the Zn-, Sn-, and Sb-mineralization have taken place in order in the Wuxu district.

(3) LA-ICP-MS U-Pb dating for cassiterties from the Jianzhupo Sb-Zn polymetallic and Bawang Zn-Fe-Sn polymetallic deposit reveal that the tin mineralization in the Wuxu district was formed at 91–90 Ma.

(4) Wuxu district have a great potential for tin mineralization. More attention should be paid for the paleokarst infilled tin-sulfide deposit in the Danchi fold-and-thrust belt, South China.

Declaration of Competing Interest

The authors declare that they have no known competing financial interests or personal relationships that could have appeared to influence the work reported in this paper.

Data availability

No data was used for the research described in the article.

Acknowledgements

This research was jointly supported by the National Natural Science Foundation of China (Grants: 41702095), the China Geological Survey (Grants: DD20190161), and the CGS Research Fund (Grants: DZLXJK202203). Richard W. Allmendinger is thanked for sharing the structural software *FaultKin* and *Stereonet*. We are also grateful for the helpful editorial review of the Editor-in-Chief Professor Hua-Yong Chen, the Associate Editor, Professor Deru Xu, and three anonymous reviewers, for their critical comments and valuable suggestions, which have significantly improved the manuscript.

Appendix A. Supplementary data

ESM Table 1 LA-ICP-MS U-Pb dating results and compositions of cassiterite from the Wuxu Sb-Zn-polymetallic district, South China. Supplementary data to this article can be found online at https://doi.org/10.1016/j.oregeorev.2022.105150.

References

Allmendinger, R.W., Cardozo, N.C., Fisher, D., 2013. Structural Geology Algorithms: Vectors & Tensors. England, Cambridge University Press, Cambridge, pp. 1–289.

Bente, K., Doering, T., 1993. Solid-state diffusion in sphalerites: an experimental verification of the "chalcopyrite disease". Eur. J. Mineral. 5 (3), 465–478.

Brooker, D.D., Craig, J.R., Rimstidt, J.D., 1987. Ore metamorphism and pyrite porphyroblast development at the Cherokee Mine, Ducktown, Tennessee. Econ. Geol. 82, 72–86.

Cai, M.H., Mao, J.W., Liang, T., Franco, P., Huang, H.L., 2007. The origin of the Tongkeng-Changpo tin deposit, Dachang metal district, Guangxi, China: clues from fluid inclusions and He isotope systematics. Minalium Deposita 42, 613–626.

Cai, M.H., Liang, T., Peng, Z.A., Fan, S,K., Luo, X.W., Mo, S.R., Zheng, Y., Xu, Y.Q., Zhang, Q., Gan, Z.W., 2014. The Geology and Mineralization of Dachang tin polymetallic orefield: Geological Pblishing House, 143 pp.

Cai, M.H., Liang, T., Wu, D.C., Huang, H.M., 2004. Structure characteristics and mineralization controls of the Nandan-Hechi metallogenic belt in Guangxi province. Geology and Prospecting 40, 5–10 in Chinese with English abstract.

Cai, M.H., Liang, T., Wu, D.C., 2005. Geological characteristics and oreforming time of the Kangma deposit in the Dachang tin polymetallic ore field. Guangxi. Acta Geol. Sin. 79, 262–268 in Chinese with English abstract.
Cai, M.H., He, L.Q., Liu, G.Q., Wu, D.C., Huang, H.M., 2006. SHRIMP zircon U-Pb dating of the intrusive rocks in the Dachang tin-polymetallic ore field, Guangxi and their geological significance. Geol. Rev. 52, 409–414 in Chinese with English abstract.
Cai, M.H., Zhao, G.C., Zheng, Y., Wang, X.B., Guo, T.F., Liu, H., 2012. Ore-controlling structural styles of the Nandan-Hechi metallogenic belt in northwestern Guangxi Province. Geology and Exploration 48, 68–75 in Chinese with English abstract.
Cardozo, N., Allmendinger, R.W., 2013. Spherical projections with OSXStereonet. Comput. Geosci. 51, 193–205.
Cawood, P.A., Zhao, G.C., Yao, J.L., Wang, W., Xu, Y.J., Wang, Y.J., 2018. Reconstructing South China in Phanerozoic and Precambrian supercontinents. Earth Sci. Rev. 186, 173–194.
Chang, J., Li, Y.Z., Zhao, J., Cai, M.H., Hu, J.G., Peng, Z.A., 2016. Characteristics of fluid inclusions of Jianzhupo Pb-Zn deposit in Wuxu ore field of Guangxi and its geological significance. Mineral Resources and Geology 30, 270–277 in Chinese with English abstract.
Charvet, J., Shu, L., Shi, Y., Guo, L., Faure, M., 1996. The building of south China: Collision of Yangzi and Cathaysia blocks, problems and tentative answers. J. SE Asian Earth Sci. 13 (3-5), 223–235.
Chen, M.H., Lu, G., Li, X.H., 2012. Muscovite $^{40}Ar/^{39}Ar$ dating of the quartz porphyry veins from Northwest Guangxi, China, and its geological significance. Geological Journal of China Universities 18, 106–116 in Chinese with English abs.
Chen, M.H., Zhang, Y., Meng, Y.Y., Lu, G., Liu, S.Q., 2014. Determination of upper limit of metallogenic epoch of Liaotun gold deposit in Western Guangxi and its implications for chronology of carlin-type gold deposits in Yunnan-Guizhou-Guangxi "Golden Triangle" area. Miner. Deposita 33, 1–13 in Chinese with English abs.
Chen, M.H., Bagas, L., Liao, X., Zhang, Z.Q., Li, Q.L., 2019. Hydrothermal apatite SIMS Th Pb dating: Constraints on the timing of low-temperature hydrothermal Au deposits in Nibao, SW China. Lithos 324–325, 418–428.
Chen, J.H., Wang, Q.F., Shu, Q.H., Weng, W.J., Xu, X.J., Wang, T.Y., Zhang, Q.Z., 2021. Geology and genesis of the Debao Cu polymetallic skarn deposit, southwestern China. Ore Geology Reviews 131, 104046.
Cheng, Y.B., Mao, J.W., Chang, Z.S., Pirajno, F., 2013. The origin of the world class tin-polymetallic deposits in the Gejiu district, SW China: Constraints from metal zoning characteristics and ^{40}Ar-^{39}Ar geochronology. Ore Geol. Rev. 53, 50–62.
Cheng, Y., Mao, J., Liu, P., 2016. Geodynamic setting of Late Cretaceous Sn-W mineralization in southeastern Yunnan and northeastern Vietnam. Solid Earth Sciences 1 (3), 79–88.
Craig, J.R., Vokes, F.M., 1993. Post-recrystallisation and ore petrography. John Wiley and Sons Press, New York, pp. 1–406.
Duan, L., Meng, Q.R., Wu, G.L., Yang, Z., Wang, J.Q., 2020. Nanpangjiang basin: A window on the tectonic development of south China during Triassic assembly of the southeastern and eastern Asia. Gondwana Res. 78, 189–209.
Dubljansky, V.N., Kiknadze, T.Z., 1983. Hydrogeology of karst of the Alpine folded region of the south of the USSR: Moscow. Nauka 1–125.
Fan, D., Zhang, T., Ye, J., Pasava, J., Kribek, B., Dobes, P., Varrin, I., Zak, K., 2004. Geochemistry and origin of tin-polymetallic sulphide deposits hosted by the Devonian black shale series near Dachang, Guangxi, China. Ore Geol. Rev. 24, 103–120.
Faure, M., Chen, Y., Feng, Z.H., Shu, L.S., Xu, Z.Q., 2017. Tectonics and geodynamics of South China: An introductory note. J. Asian Earth Sci. 141, 1–6.
Fu, M., Changkakoti, A., Krouse, H.R., Gray, J., Kwak, T.A.P., 1991. An oxygen, hydrogen, sulphur, and carbon isotope study of carbonate-replacement (skarn) tin deposits of the Dachang tin field, Chinap. Econ. Geol. 86, 1683–1703.
Fu, M., Kwak, T.A.P., Mernagh, T.P., 1993. Fluid inclusion studies of zoning in the Dachang tin-polymetallic ore field, People's Republic of China. Econ. Geol. 88, 283–300.
Gao, T., 2020. Caledonian episodes in Youjiang Basin, southeastern margin of the Yangtze plate. China University of Geosciences (in Chinese with English abstract). M. S. thesis.
Gao, W., Hu, R.Z., Hofstra, A.H., Li, Q.L., Zhu, J.J., Peng, K.Q., Mu, L., Huang, Y., Ma, J. W., Zhao, Q., 2021. U-Pb dating on hydrothermal rutile and monazite from the Badu gold deposit supports an Early Cretaceous age for Carlin-type gold mineralization in the Youjiang basin, Southweatern China. Econ. Geol. 116, 1355–1385.
Guo, J., Zhang, R.Q., Sun, W.D., Ling, M.X., Hu, Y.B., Wu, K., Luo, M., Zhang, L.C., 2018. Genesis of tin-dominant polymetallic deposits in the Dachang district, South China: Insights from cassiterite U-Pb ages and trace element compositions. Ore Geol. Rev. 95, 863–879.
Guo, J., Wu, K., Seltmann, R., Zhang, R., Ling, M., Li, C., Sun, W., 2021. Unraveling the link between mantle upwelling and formation of Sn-bearing granitic rocks in the world-class Dachang tin district, South China. GSA Bulletin 134, 1043–1064.
Han, F., Zhao, R.S., Shen, J.Z., Hutchinson, R.W., Jiang, S.Y., Chen, H.D., 1997. Geology and Origin of Ores in the Dachang tin-Polymetallic Ore Field. Geological Publishing House, Beijing 1–213 in Chinese with English abstract.
Hao, S., 2012. Metallotectionical tectionical Types and their Evolution of the Metallotectionical tectionical Types and their Evolution of the. Guilin University of Technology (in Chinese with English abstract). M.S. thesis.
Huang, W.T., Liang, H.Y., Zhang, J., Wu, J., Chen, X.L., Ren, L., 2019. Genesis of the Dachang Sn-polymetallic and Baoshan Cu ore deposits, and formation of a Cretaceous Sn-Cu ore belt from southwest China to western Myanmar. Ore Geol. Rev. 112, 103030.
Jiang, S.Y., Han, F., Shen, J.Z., Palmer, M.R., 1999. Chemical and Rb-Sr, Sm-Nd isotopic systematics of tourmaline from the Dachang Sn-polymetallic ore deposit, Guangxi Province, PR China. Chem. Geol. 157, 49–67.
Keith, M., Haase, K.M., Schwarz-Schampera, U., Klemd, R., Petersen, S., Bach, W., 2014. Effects of temperature, sulfur, and oxygen fugacity on the composition of sphalerite from submarine hydrothermal vents. Geology 42, 699–702.
Kwak, T.A.P., 1987. W-Sn skarn deposits and related metamorphic skarns and granitoids. Developments in Economic Geology, Elsevier Science Ltd.
Lepvrier, C., Maluski, H., Tich, V.V., Leyreloup, A., Thi, P.T., Vuong, N.V., 2004. Early Triassic Indochina orogeny in Vietnam (Truong Son Belt and Kontum Massif): implications for the geodynamic evolution of Indochina. Tectonophysics 393, 87–118.
Li, J.H., Dong, S.W., Cawood, P.A., Zhao, G.C., Johnston, S.T., Zhang, Y.Q., Xin, Y.J., 2018. An Andean-type retro-arc foreland system beneath northwest South China revealed by SINOPROBE profiling. Earth Planet. Sci. Lett. 490, 170–179.
Li, J.H., Cawood, P.A., Ratschbacher, L., Zhang, Y.Q., Dong, S.W., Xin, Y.J., Yang, H., Zhang, P.X., 2020. Building Southeast China in the late Mesozoic: Insights from alternating episodes of shortening and extension along the Lianhuashan fault zone. Earth Sci. Rev. 201, 103056.
Li, S.Z., Li, X.Y., Zhao, S.J., Yang, Z., Liu, X., Guo, L.L., Wang, Y.M., Hao, Y., Zhang, J., Hu, M.Y., 2016. Global Early Paleozoic Orogens (III): Intracontinental ogeogen in South China. Journal of Jilin University (Earth Science Edition). 46, 1005–1025 in Chinese with English abstract.
Li, S.Z., Suo, Y.H., Li, X.Y., Zhou, J., Santosh, M., Wang, P.P., Wang, G.Z., Guo, L.L., Yu, S.Y., Lan, H.Y., Dai, L.M., Zhou, Z.Z., Cao, X.Z., Zhu, J.J., Liu, B., Jiang, S.H., Wang, G., Zhang, G.W., 2019. Mesozoic tectono-magmatic response in the East Asian ocean-continentconnection zone to subduction of the Paleo-Pacific Plate. Earth Sci. Rev. 192, 91–137.
Li, H.Q., Wang, D.H., Mei, Y.P., Liang, T., Chen, Z.Y., Guo, C.L., Ying, L.J., 2008. Lithogenesis and mineralization chronology study on the lamo zinc-copper polymetallic ore deposit in Dachang orefield. Guangxi. Acta Geol. Sin. 82, 912–920 in Chinese with English abstract.
Liang, T., Wang, D.H., Hou, K.J., Li, H.Q., Huang, H.M., Cai, M.H., Wang, D.M., 2011. LA-MC-ICP-MS zircon U-Pb dating of Longxianggai pluton in Dachang of Guangxi and its geological significance. Acta Petrologica Sinica 27, 1624–1636 in Chinese with English abstract.
Liu, Y.S., Hu, Z.C., Gao, S., Günther, D., Xu, J., Gao, C.G., Chen, H.H., 2008. In situ analysis of major and trace elements of anhydrous minerals by LA-ICP-MS without applying an internal standard. Chem. Geol. 257, 34–43.
Liu, Y.B., Zhang, L.F., Mo, X.X., Santosh, M., Dong, G.C., Zhou, H.Y., 2020b. The giant tin polymetallic mineralization in southwest China: Integrated geochemical and isotopic constraints and implications for Cretaceous tectonomagmatic event. Geosci. Front. 11, 1593–1608.
Liu, T.T., Zhu, C.W., Wang, D.P., Zhang, S.G., Zhang, Q.B., Chen, C.Y., Wang, G.H., 2020a. Genesis of the Jianzhupo Pb-Zn-Sb polymetallic deposit in the Wuxu in the Wuxu ore field, Guangxi province: Constrains from sulfur isotopes of sulfides and trace elements compositions of sphalerites. Bulletin of Mineralogy, Petrology and Geochemistry 39, 646–662 in Chinese with English Abstract.
Ludwing, K.R., 2008. User's manual for isoplot 3.17: A geochronological toolkit for Microsoft Excel. Berkeley Geochronology Center, Special Publication 4, 5–72.
Maeshall, B., Gilligan, L.B., 1987. An introduction to remobilization: Information from ore-body geometry and experimental considerations. Ore Geol. Rev. 2, 87–131.
Maluski, H., Lepvrier, C., Jolivet, L., Carter, A., Roques, A., Beyssac, O., Tang, T.T., Thang, N.D., Avigad, D., 2001. Ar-Ar and fission-track ages in the Song Chay Massif: Early Triassic and Cenozoic tectonics in northern Vietnam. J. Asian Earth Sci. 19, 233–248.
Mao, J.W., Ouyang, H.G., Song, S.W., Santosh, M., Yuan, S.D., Zhou, Z.H., Zheng, W., Liu, H., Liu, P., Cheng, Y.B., Chen, M.H., 2019. Geology and metallogeny of tungsten and tin deposits in China. SEG Special Publications 22, 411–482.
Mao, J.W., Zheng, W., Xie, G.Q., Lehmann, B., Goldfarb, R., 2020. Recognition of a Middle-Late Jurassic arc-related porphyry copper belt along the southeast China coast: Geological characteristics and metallogenic implications. Geology 49, 592–596.
Mao, J.W., Liu, P., Goldfarb, R.J., Goryachev, N.A., Pirajno, F., Zhang, W., Zhou, M.F., Zhao, C., Xie, G.Q., Yuan, S.D., Liu, M., 2021. Cretaceous large–scale metal accumulation triggered by post–subductional large–scale extension. East Asia. Ore Geology Reviews 136, 104270.
Marrett, R.A., Allmendinger, R.W., 1990. Kinematic analysis of fault-slip data. J. Struct. Geol. 12, 973–986.
Nagashima, M., Akasaka, M., Morifuku, Y., 2016. Ore and skarn mineralogy of the Yamato Mine, Yamaguchi Prefecture, Japan, with emphasis on silver-, Bismuth-, Cobalt-, and tin-bearing sulfides. Resour. Geol. 66, 37–54.
Nevolko, P.A., Hoa, T.T., Redin, Y.O., Anh, T.T., Phuong, N.T., Ly, V.H., Dultsev, V.F., Dung, P.T., Huong, N.T., 2017. Geology, mineralogy, geochemistry and $\delta^{34}S$ of sedimentary rock-hosted Au deposits in Song Hien structure. NE Vietnam: Ore Geology Reviews 84, 273–288.
Patterson, D.J., Ohmoto, H., Solomon, M., 1981. Geologic setting and genesis of cassiterite-sulfide mineralization at Renison Bell, western Tasmania: Econ. Geol. 76, 393–438.
Peng, Z., Watanabe, M., Hoshino, K., 1997. Overview of tin-bearing polymetallic mineralisation in the Dachang ore field. Resour. Geol. 47, 331–341.
Qiao, L., 2016. Tectonic Evolution and Bauxite Metallogenesis in the Youjiang Basin and Adjacent Area. China University of Geosciences (in Chinese with English abstract). Ph.D. thesis.
Scott, S.D., 1983. Chemical behaviour of sphalerite and arsenopyrite in hydrothermal and metamorphic environments. Mineral. Mag. 47, 427–435.
Scott, S.D., Barnes, H.L., 1971. Sphalerite geothermometry and geobarometry. Econ. Geol. Bull. Soc. Econ. Geol. 66, 653–669.

Shimizu, M., Shikazono, N., 1985. Iron and zinc partitioning between coexisting stannite and sphalerite: a possible indicator of temperature and sulfur fugacity. Miner. Deposita 20, 314–320.
Shu, L.S., Yao, J.L., Wang, B., Faure, M., Charvet, J., Chen, Y., 2021. Neoproterzoic plate tectonic process and Phanerozoic geodynamic evolution of the South China Block. Earth Sci. Rev. 216, 103596.
Sichuan Shanhe Assets Evaluation Co., Ltd (SCSH). 2021. The report of assets evaluation of mining rights sale revenue for No. I orebody from the Bawang Sn-Zn deposit, Jinchengjiang district, Guangxi province, China. 1–48, http://dnr.gxzf.gov.cn/show?id=76700.
Smith, M.T., Rhys, D., Ross, K., Lee, C., Gray, J.N., 2013. The Long Canyon Deposit: Anatomy of a New Off-Trend Sedimentary Rock-Hosted Gold Discovery in Northeastern Nevada. Econ. Geol. 108, 1119–1145.
Su, W.C., Hu, R.Z., Xia, B., Xia, Y., Liu, Y.P., 2009. Calcite Sm-Nd isochron age of the Shuiyindong Carlin-type gold deposit, Guizhou, China. Chem. Geol. 258, 269–274.
Su, Y.R., Li, Y.S., Qin, D.X., 2007. Foundation on model of ore-forming of orebody 100 for the Dachang orefield in Guangxi province. Nonferrous Metals (Mining Section) 59, 21–25 in Chinese with English abstract.
Suo, Y.H., Li, S.Z., Cao, X.Z., Wang, X.Y., Somerville, I., Wang, G.Z., Wang, P.C., Liu, B., 2020. Mesozoic-Cenozoic basin inversion and geodynamics in East China: A review. Earth Sci. Rev. 210, 103357.
Tang, Y.W., Cui, K., Zheng, Z., Gao, J.F., Han, J.J., Yang, J.H., Liu, L., 2020. LA-ICP-MS U-Pb geochronology of wolframite by combining NIST series and common lead-bearing MTM as the primary reference material: Implications for metallogenesis of South China. Gondwana Res. 83, 217–231.
Tang, Y.W., Gao, J.F., Lan, T.G., Cui, K., Han, J.J., Zhang, X., Chen, Y.W., Chen, Y.H., 2021. In situ low-U garnet U-Pb dating by LA-SF-ICP-MS and its application in constraining the origin of Anji skarn system combined with Ar-Ar dating and Pb isotopes. Ore Geol. Rev. 130, 103970.
U.S. Geological Survey, 2021. Mineral Commodity Summaries 2021. U.S. Geological Survey 1–200. https://pubs.er.usgs.gov/publication/mcs2021.
Wang, D.M., 2012. A Study on the characteristic and Origin of the Antimony Deposit in Danchi Metallogenic Belt, Guangxi. Chang'an University (in Chinese with English abstract). Ph.D. thesis.
Wang, D.H., Chen, Y.C., Chen, W., Sang, H.Q., Li, H.Q., Lu, Y.F., Chen, K.L., Lin, Z.M., 2004. Dating of the Dachang Superlarge Tin-polymetallic deposit in Guangxi and Its implication for the genesis of the No. 100 Orebody. Acta Geol. Sin. 78, 452–458 in Chinese with English abstract.
Wang, X.Y., Huang, H.W., Chen, N.S., Huang, X.Q., Wu, X.K., Hao, S., Li, H.M., 2015. In-situ LA-MC-ICPMS U-Pb Geochronology of cassiterite from Changpo-Tongkeng tin-polymetallic deposits, Dachang orefield. Guangxi. Geol. Rev. 61, 892–900 in Chinese with English abstract.
Wang, T.Y., Li, G.J., Wang, Q.F., Santosh, M., Zhang, Q.Z., Deng, J., 2019. Petrogenesis and metallogenic implications of Late Cretaceous I- and S-type granites in Dachang-Kunlunguan ore belt, southwestern South China Block. Ore Geol. Rev. 113, 103079.
Wang, Y.N., Li, G.J., Wang, Q.F., Santosh, M., Chen, J.H., 2020b. Early Paleozoic granitoids from South China: implications for understanding the Wuyu-Yunkai orogen. Int. Geol. Rev. 62, 243–261.
Wang, Y.J., Wang, Y., Zhang, Y.Z., Cawood, P.A., Qian, X., Gan, C.S., Zhang, F.F., Zhang, P.Z., 2021. Triassic two-stage intra-continental orogensis of the South China Block, driven by Paleotethyan closure and interactions with adjoining blocks. J. Asian Earth Sci. 206, 104648.
Wang, Q.F., Yang, L., Xu, X.J., Santosh, M., Wang, Y.N., Wang, T.Y., Chen, F.G., Wang, R. X., Gao, L., Liu, X.F., Yang, S.J., Zeng, Y.S., Chen, J.H., Zhang, Q.Z., Deng, J., 2020a. Multi-stage tectonics and metallogeny associated with Phanerozoic evolution of the South China Block: A holistic perspective from the Youjiang Basin. Earth Sci. Rev. 211, 103405.
Wu, J., Yuan, H.W., Gan, N.J., Wei, S.C., Liao, J., Zhang, J., Liang, H.Y., 2020. Source characteristics of magmatic rocks and zircon U-Pb age in the Mangchang orefield, Danchi metallogenic belt, Guangxi. Acta Petrologica Sinica 36, 1586–1596 in Chinese with English abstract.
Wu, Y., Zhang, S., Huang, Z., Wang, F.G., Li, J.X., Xiao, C.H., Ye, J.L., Zhang, C., 2019. Meso-Cenozoic Tectonic Evolution of the Nandan-Libo area, Northwestern Guangxi, China: Evidence from Paleo-tectonic stress fields analyses. Geotectonic et Metallogenia 43, 872–893 in Chinese with English abstract.
Xiao, C.H., 2018. Characteristics of Ore-controlling Structures and the Dynamic Setting of the Danchi Metallogenic Belt, South China. Published Post-doctor work report, Beijing, China, China University of Geosciences, 1–109 (in Chinese with English abstract).
Xiao, C.H., Shen, Y.K., Liu, H., Wei, C.S., Le, X.W., Fu, B., 2018a. Oxygen isotopic compositions and geological significance of zircons from the Yanshanian felsic intrusions in the Xidamingshan cluster, southeastern margin of the Youjiang fold belt, South China: In situ SHRIMP analysis. Acta Petrologica Sinica 34, 1441–1452 in Chinese with English abstract.
Xiao, C.H., Shen, Y.K., Wei, C.S., Su, X.K., Le, X.W., Zhang, L., 2018b. LA-ICP-MS zircon U-Pb dating, Hf isotopic composition and Ce^{4+}/Ce^{3+} characteristics of the Yanshanian acid magma in the Xidamingshan cluster, southeastern margin of the Youjiang fold belt, Guangxi. Geoscience 32, 289–304 in Chinese with English abstract.
Yao, Y.S., Qing, Z.C., 2002. Study of ore compositions in No. 100 orebody of Dachang cassiterite-polymetallic sulfide deposit of Guangxi. Mineral Resources and Geology 16, 281–286 in Chinese with English abstract.
Ye, X.S., Pan, Q.Y., 1994. Discovery history of Dachang tin-polymetallic orefield, Nandan County. Guangxi. Guangxi Geol. 7, 85–94 in Chinese with English abstract.
Yuan, S.D., Peng, J.T., Hao, S., Li, H.M., Geng, J.Z., Zhang, D.L., 2008. A precise U-Pb age on cassiterite from the Xianghualing tin-polymetallic deposit (Hunan, South China). Miner. Deposita 43, 375–382.
Zeng, Y.F., Liu, W.J., Chen, H.D., Zheng, J.Q., Li, X.Q., Jiang, T.C., 1995. Evolution of sedimentation and tectonics of the Youjiang composite basin. South China. Acta Geol. Sin. 69, 113–124 in Chinese with English abstract.
Zhang, G.W., Guo, A.L., Wang, Y.J., Li, S.Z., Dong, Y.P., Liu, S.F., He, D.F., Cheng, S.Y., Lu, H.K., Yao, A.P., 2013. Tectonics of South China continent and its implications. Science China: Earth Sciences 56, 1804–1828 in Chinese with English abstract.
Zhang, J., Huang, W.T., Liang, H.Y., Wu, J., Chen, X.L., 2018. Genesis of the Jianzhupo Sb–Pb–Zn–Ag deposit and formation of an ore shoot in the Wuxu ore field, Guangxi, South China. Ore Geol. Rev. 102, 654–665.
Zhang, X.T., Zhang, R.H., Hu, S.M., 2014. Tin transportation experiments in high temperature vapour phase and mechanism of forming No. 100 ore body in Dachang. Nanling. Acta Geologica Sinica 88, 716–735 in Chinese with English abstract.
Zhao, K.D., 2003. Isotope geochemistry and genetic models of two types of tin deposits: case studies from the Dachang and the Furong tin deposits. Nanjing University (in Chinese with English abstract). Ph.D. thesis.
Zhao, Y., Huang, L.S., Tang, Y.P., Wang, J.C., Wu, X.L., Liu, W., 2020. Prospecting prediction and exploration of the deep concealed rock mass in Wuxu anti ony polymentallic ore field, Guangxi. Mineral Resources and Geology 34, 109–114 in Chinese with English abstract.
Zhao, K.D., Zhang, L.H., Palmer, M.R., Jiang, S.Y., Zhao, H.D., Chen, W., 2021. Chemical and boron isotopic compositions of tourmaline at the Dachang Sn-polymetallic ore district in South China: Constraints on the origin and evolution of hydrothermal fluids. Miner. Deposita 56, 1589–1608.
Zhou, X.Y., Yu, J.H., O'Relly, S.Y., Griffin, W.L., Wang, X.L., Sun, T., 2017. Sources of the Nanwenhe-Song Chay granitic complex (SW China-NE Vietnam) and its tectonic significance. Lithos 290–291, 76–93.
Zhu, J.J., Zhong, H., Xie, G.Q., Zhao, C.H., Xu, L.L., Lu, G., 2016. Origin and geological implication of the inherited zircon from felsic dykes, Youjiang basin, China. Acta Petrol. Sin. 32, 3269–3280 in Chinese with English abstract.